A Multimoment Finite-Volume Shallow-Water Model on the Yin–Yang Overset Spherical Grid

XINGLIANG LI

Tokyo Institute of Technology, Yokohama, Japan, and State Key Laboratory of Severe Weather, Chinese Academy of Meteorological Sciences, Beijing, China

DEHUI CHEN

State Key Laboratory of Severe Weather, Chinese Academy of Meteorological Sciences, Beijing, China

XINDONG PENG* AND KEIKO TAKAHASHI

Earth Simulator Center, JAMSTEC, Yokohama, Japan

FENG XIAO

Institute of Mechanics, Chinese Academy of Sciences, Beijing, China, and Tokyo Institute of Technology, Yokohama, Japan

(Manuscript received 26 March 2007, in final form 7 November 2007)

ABSTRACT

A numerical model for shallow-water equations has been built and tested on the Yin–Yang overset spherical grid. A high-order multimoment finite-volume method is used for the spatial discretization in which two kinds of so-called moments of the physical field [i.e., the volume integrated average (VIA) and the point value (PV)] are treated as the model variables and updated separately in time. In the present model, the PV is computed by the semi-implicit semi-Lagrangian formulation, whereas the VIA is predicted in time via a flux-based finite-volume method and is numerically conserved on each component grid. The concept of including an extra moment (i.e., the volume-integrated value) to enforce the numerical conservativeness provides a general methodology and applies to the existing semi-implicit semi-Lagrangian formulations. Based on both VIA and PV, the high-order interpolation reconstruction can only be done over a single grid cell, which then minimizes the overlapping zone between the Yin and Yang components and effectively reduces the numerical errors introduced in the interpolation required to communicate the data between the two components. The present model completely gets around the singularity and grid convergence in the polar regions of the conventional longitude–latitude grid. Being an issue demanding further investigation, the high-order interpolation across the overlapping region of the Yin–Yang grid in the current model does not rigorously guarantee the numerical conservativeness. Nevertheless, these numerical tests show that the global conservation error in the present model is negligibly small. The model has competitive accuracy and efficiency.

1. Introduction

In the past decade, some sophisticated numerical algorithms that were originally developed and used in the computational fluid dynamics (CFD) community have been introduced and getting an increasing popularity in global atmospheric and oceanic modeling. Among the representative ones are the spectral-element (SE) method (Thomas and Loft 2002; Giraldo and Rosmond 2004) and the discontinuous Galerkin (DG) method (Nair et al. 2005a). Although these methods usually require more computational effort than the conventional finite-difference or finite-volume methods, their superiority in numerical accuracy and convergence motivates the further exploration to implement them in geophysical fluid simulations.

* Current affiliation: State Key Laboratory of Severe Weather, Chinese Academy of Meteorological Sciences, Beijing, China.

Corresponding author address: Feng Xiao, Department of Energy Sciences, Tokyo Institute of Technology, 4259 Nagatsuta, Midori-ku, Yokohama, 226-8502, Japan.
E-mail: xiao@es.titech.ac.jp

DOI: 10.1175/2007MWR2206.1

We have recently developed a general numerical framework, the so-called Constrained Interpolation Profile/Multimoment Finite-Volume Method (CIP/MM FVM; Yabe et al. 2001; Xiao and Yabe 2001; Xiao 2004; Xiao et al. 2006a; Ii and Xiao 2007) for CFD applications. The basic idea of the CIP/MM method is to make use of more than one moments, which are in fact the volume-integrated average (VIA) and the point value (PV) in the present model for a physical field when constructing the spatial numerical approximations, and to treat all the moments as the model variables that are integrated forward in time separately. Based on multimoments, the high-order interpolation can be constructed over single grid cell. The CIP/MM FVM has a great flexibility in updating different moments (i.e., different moments can be computed by different numerical methods). In the present work, the PV, which is not necessarily conserved, is updated by a semi-Lagrangian and semi-implicit numerical procedure that has been widely used in meteorological modeling. The conservative moment VIA on the other hand is advanced through a flux-based finite-volume formulation (or equivalently a volume remapping). The resultant numerical algorithm can be interpreted as a combination of the semi-implicit semi-Lagrangian method and a finite-volume method, where one of the moments (VIA) is numerically conserved, and is quite simple and easy to implement. Different numerical dispersion can also be obtained from the multimoment formulation. Xiao et al. (2006b), for example, discussed the numerical dispersion of the simplest multimoment finite-volume method for the geostrophic adjustment.[1]

Another problem associating the construction of the global circulation model comes from the numerical representation of the spherical geometry. Because of the singularity and the convergence of meridians in the polar regions of the longitude–latitude grid system, other alternatives that share more uniform grid spacing are recently explored, for instance, the icosahedral geodesic grid (Heikes and Randall 1995; Stuhne and Peltier 1999; Tomita et al. 2001; Majewski et al. 2002) and the gnomonic-cubic grid (Sadourny 1972; Rančić et al. 1996; Ronchi et al. 1996; McGregor 1997). Being a Chimera grid, the Yin–Yang grid (see Fig. 1) was suggested by Kageyama and Sato (2004) as a quasi-uniform overset grid free from the polar singularity. A Yin–Yang grid is constructed by overlapping two perpendicularly oriented longitude–latitude grid components of the low-latitude part. With each of its component being part of the conventional longitude–latitude grid, the Yin–Yang grid provides a convenient platform readily to accommodate the numerical works originally developed for the latitude–longitude grid. Li et al. (2006) developed an accurate semi-Lagrangian scheme on the Yin–Yang grid by using a high-order interpolation for the overlapping region. However, the interpolation for communicating data across the Yin–Yang border usually does not guarantee the numerical conservativeness. Peng et al. (2006) proposed an exactly conservative advection transport scheme on the Yin–Yang grid based on a piecewise constant reconstruction. For higher-order approximations or the general system of conservative equations for fluid dynamics, the complete conservativeness across the Yin–Yang overlapping region requires more complicated numerics. Nevertheless, as shown in this paper, using a conservative numerical scheme for each individual grid component and minimizing the overlapping zone, one can still obtain adequate, even if not rigorous, conservativeness for medium-range weather prediction or short-range climate simulation.

In this paper, we will implement the CIP/MM FVM on the Yin–Yang grid. All the computations on each individual grid component are exactly conserved and the halo layer in the overlapping region is minimized by the multimoment reconstruction. This paper is organized as follows. The Yin–Yang grid is briefly described in section 2. Section 3 presents the spatial discretization based on two kinds of moments (i.e., PV and VIA) in two-dimensional longitude–latitude grid. The time integration scheme for the shallow-water equation is discussed in section 4. The semi-implicit/semi-Lagrangian procedure (McDonald and Bates 1989) is adopted to compute the PVs. With the PVs updated, the VIAs are simply predicted by evaluating the numerical fluxes in terms of the PVs averaged over two time steps. The scheme for advection is briefly presented in section 5. The model is verified in section 6 by a series of widely used benchmark tests. We present our conclusions in section 7.

2. Yin–Yang grid

The Yin–Yang grid (Kageyama and Sato 2004) is an overset grid for spherical geometry, which consists of

[1] We should notify another solution of the dispersion equation of the M grid in Xiao et al. (2006b) as follows [see Xiao et al. (2006b) for notation description]:

$$\left(\frac{\sigma}{f}\right)^2 = \frac{1}{2} + 2\gamma - \sqrt{\left(\frac{1}{2} - 2\gamma\right)^2 + \epsilon}.$$

It is observed that this mode has a frequency significantly lower than that of the physical one discussed in Xiao et al. (2006b). From the numerical experiments carried out so far, we have not found a significant effect of thiscomputational mode on the numerical solutions.

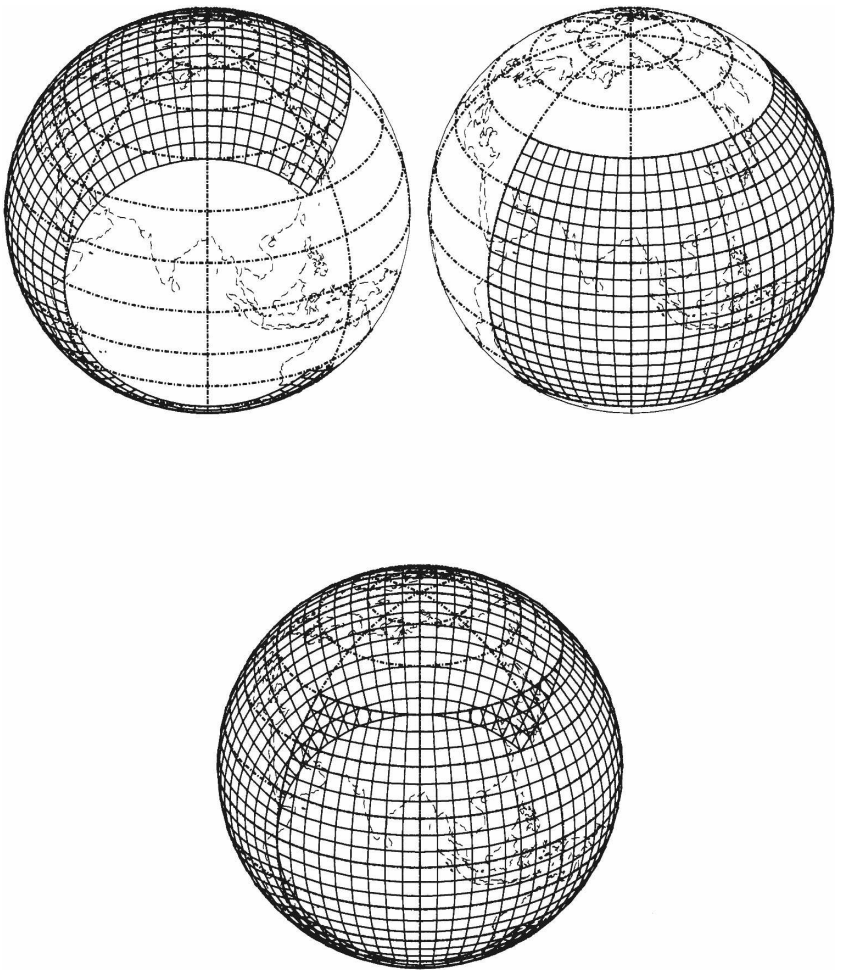

FIG. 1. (bottom) Schematic diagram of the Yin–Yang grid, which consists of two notched lon-lat grids [i.e., (top left) Yin grid and (top right) Yang grid] perpendicularly oriented to each other. Each component grid covers a domain of longitudinal 270° and latitudinal 90°.

two notched longitude–latitude grids normal to each other (Fig. 1). The component (Yin or Yang) grid is selected to be the low-latitude part of the longitude–latitude grid. The composition of the two component grids, with one of the components being perpendicular to the other, covers the globe with an overlapping zone where the data need to be communicated between the two components during the computation.

The relationship between the Yin coordinate and the Yang coordinate is easily found by considering any position vector in the Cartesian coordinates (X, Y, Z) as

$$(X^n, Y^n, Z^n) = (-X^e, Z^e, Y^e), \tag{1}$$

where the superscript n denotes the Yang coordinate and e is the Yin coordinate.

From Eq. (1), we have the relationship in the spherical coordinate (λ, φ):

$$\cos\varphi^n \cos\lambda^n = -\cos\varphi^e \cos\lambda^e, \tag{2}$$

$$\cos\varphi^n \sin\lambda^n = \sin\varphi^e, \quad \text{and} \tag{3}$$

$$\sin\varphi^n = \cos\varphi^e \sin\lambda^e. \tag{4}$$

In this paper, the computational domain (Yin or Yang grid) is defined to be from 45°S to 45°N in the latitudinal direction and from 45° to 315°E in the longitudinal direction. As we can see from the next section, the spatial reconstruction based on multimoments can be done over a single computational cell, thus the overlapping zone of the Yin–Yang grid used here is minimized.

The grid partitioning for both Yin and Yang components are

$$\varphi_j^l = \varphi_{\min} + j\Delta\varphi, \quad (j = 0, N_\varphi - 1) \quad \text{and}$$
$$\lambda_i^l = \lambda_{\min} + i\Delta\lambda, \quad (i = 0, N_\lambda - 1), \tag{5}$$

with

$$\Delta\varphi = (\varphi_{\max} - \varphi_{\min})/(N_\varphi - 1) \quad \text{and}$$
$$\Delta\lambda = (\lambda_{\max} - \lambda_{\min})/(N_\lambda - 1), \tag{6}$$

where l represents n (Yang grid) or e (Yin grid). As mentioned before, the domain bounds of the two components are specified, respectively, as $\varphi_{\min} = -\pi/4$, $\varphi_{\max} = \pi/4$, $\lambda_{\min} = \pi/4$, and $\lambda_{\max} = 7\pi/4$. Here N_φ and N_λ denote the total grid points in the latitude and longitude directions, respectively.

As an overset grid, the interpolation is needed between the Yin and Yang grid to communicate data. For scalar variables, the data transfer between the Yin and Yang grids is straightforward as long as the interpolation in the overlapping region is properly constructed. However, extra attention must be paid when one communicates a vector field since the expressions of a vector in the Yin and Yang spherical coordinates are different.

The transformation of a horizontal vector $\mathbf{v} = (u, v)$ between Yin and Yang components is given as

$$\begin{pmatrix} v^n \\ u^n \end{pmatrix} = \mathbf{P}\begin{pmatrix} v^e \\ u^e \end{pmatrix}, \tag{7}$$

where the projection matrix $\mathbf{P}$ is

$$\mathbf{P} = \begin{pmatrix} -\sin\lambda^e \sin\lambda^n & -\cos\lambda^e/\cos\varphi^n \\ \cos\lambda^e/\cos\varphi^n & -\sin\lambda^e \sin\lambda^n \end{pmatrix}. \tag{8}$$

Because of the symmetry in the two components, the inverse transformation from Yin into Yang is

$$\begin{pmatrix} v^e \\ u^e \end{pmatrix} = \mathbf{P}^{-1}\begin{pmatrix} v^n \\ u^n \end{pmatrix}, \tag{9}$$

where

$$\mathbf{P}^{-1} = \begin{pmatrix} -\sin\lambda^n \sin\lambda^e & -\cos\lambda^n/\cos\varphi^e \\ \cos\lambda^n/\cos\varphi^e & -\sin\lambda^n \sin\lambda^e \end{pmatrix}. \tag{10}$$

It is worth noting that each component grid is nothing but part of the conventional longitude–latitude grid, so numerical techniques developed for the latter can be transplanted to the Yin–Yang grid very conveniently. Moreover, since only the lower-latitude part of the longitude–latitude grid is used for both the Yin and Yang components, the grid spacing of the Yin–Yang grid is quite uniform. In fact, the ratio of the minimum and the maximum grid spacing is approximately 0.707.

Bearing in mind that the Yin and Yang components are identical to a longitude–latitude coordinate, we limit our discussions in the following sections only to the Yang grid.

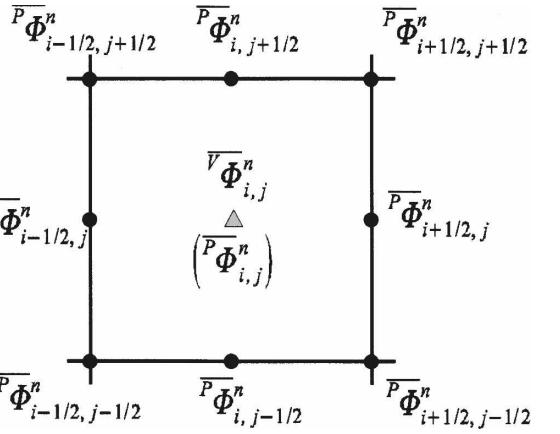

FIG. 2. The locations of the moments on a control volume. Eight PVs are defined at the vertices and middle points of boundary edges, denoted as the solid dots. The VIA is defined over the whole control volume. The point value $\overline{P\Phi}_{ij}$ at the volume center, denoted by the shaded triangle, is not an independent moment but is needed in the semi-implicit semi-Lagrangian computation and is evaluated from the multimoment reconstruction $F_{ij}(\xi, \eta)$.

3. Spatial reconstruction based on multimoments

The basic idea of the CIP/MM method is that one can make use of more than one kind of moment to describe the spatial variation of a given physical field and predict all the moments in time as model variables. In the present paper, we use two kinds of moments (i.e., the VIA and the PV).

Considering a general two-dimensional control volume (mesh cell) $\Omega_{ij} \equiv [\xi_{i-1/2}, \xi_{i+1/2}] \otimes [\eta_{j-1/2}, \eta_{j+1/2}]$ shown in Fig. 2, two kinds of moments are defined, respectively, for the field variable $\Phi(\xi, \eta)$. When applying this to the longitude–latitude grid, one just needs to switch ξ to λ and η to φ.

The VIA is defined over the control volume Ω_{ij} as

$$\overline{V\Phi}_{i,j} = \frac{1}{\Delta\xi_i \Delta\eta_j} \int_{\xi_{i-1/2}}^{\xi_{i+1/2}} \int_{\eta_{j-1/2}}^{\eta_{j+1/2}} \Phi(\xi, \eta)\, d\xi\, d\eta, \quad \text{where}$$
$$\Delta\xi_i = \xi_{i+1/2} - \xi_{i-1/2} \quad \text{and} \quad \Delta\eta_j = \eta_{j+1/2} - \eta_{j-1/2}. \tag{11}$$

Eight PVs are defined at the four vertices and the middle points of the four boundary edges of Ω_{ij} as

$$\overline{P\Phi}_{\zeta,\vartheta} = \Phi(\xi_\zeta, \eta_\vartheta), \tag{12}$$

with (ζ, ϑ) being $(i - \frac{1}{2}, j - \frac{1}{2})$, $(i, j - \frac{1}{2})$, $(i + \frac{1}{2}, j - \frac{1}{2})$, $(i - \frac{1}{2}, j)$, $(i + \frac{1}{2}, j)$, $(i - \frac{1}{2}, j + \frac{1}{2})$, $(i, j + \frac{1}{2})$, and $(i + \frac{1}{2}, j + \frac{1}{2})$, respectively.

Given one VIA and eight PVs as in Eqs. (11) and (12), a 2D quadratic polynomial for interpolation reconstruction,

$$F_{i,j}(\xi,\eta) = C_{00} + C_{10}(\xi-\xi_{i-1/2}) + C_{20}(\xi-\xi_{i-1/2})^2 + C_{01}(\eta-\eta_{j-1/2}) + C_{02}(\eta-\eta_{j-1/2})^2 + C_{11}(\xi-\xi_{i-1/2})(\eta-\eta_{j-1/2}) + C_{12}(\xi-\xi_{i-1/2})(\eta-\eta_{j-1/2})^2 + C_{21}(\xi-\xi_{i-1/2})^2(\eta-\eta_{j-1/2}) + C_{22}(\xi-\xi_{i-1/2})^2(\eta-\eta_{j-1/2})^2, \quad (13)$$

can be built over the single cell Ω_{ij}. The coefficients of interpolation function can be determined immediately by using the constraint conditions. Further details may be found in the appendix

The piecewise interpolation reconstruction function $F_{i,j}(\xi, \eta)$ will be then used in finding the departure point values in the semi-Lagrangian updating and other spatial discretizations. As will be seen later, defining two kinds moments on a single cell does not only allow us to construct high-order reconstruction interpolation with compact mesh stencil, but more importantly, it provides us with a framework to compute the PVs efficiently through the semi-Lagrangian method and to update the VIA with numerical conservativeness.

4. Time integration for the shallow-water equations

As discussed above, the CIP/MM FVM keeps both VIA and PV as the model variables that need to be predicted in time. We use different forms of the shallow-water equations as the governing equations for each of them (i.e., the advective form for the PV moment and the conservative form for the VIA moment).

a. The governing equations for PV and VIA moments

The advective form (or primitive form) of the shallow-water equations in longitude–latitude grid are written as

$$\frac{du}{dt} = -\frac{1}{a\cos\varphi}\frac{\partial}{\partial\lambda}(gh - cD) + fv + N_u, \quad (14)$$

$$\frac{dv}{dt} = -\frac{1}{a}\frac{\partial}{\partial\varphi}(gh - cD) - fu + N_v, \quad \text{and} \quad (15)$$

$$\frac{dh_w}{dt} = -h_w D, \quad (16)$$

where a is the Earth radius. The horizontal wind components along the latitude and longitude are defined as $u \equiv (d/dt)(a\cos\lambda)$ and $v \equiv (d/dt)(a\varphi)$, respectively. The divergence D is expressed by

$$D = \frac{1}{a\cos\varphi}\left[\frac{\partial u}{\partial\lambda} + \frac{\partial}{\partial\varphi}(v\cos\varphi)\right].$$

The substantial derivative is given by

$$\frac{d}{dt}() = \frac{\partial}{\partial t}() + \frac{u}{a\cos\varphi}\frac{\partial}{\partial\lambda}() + \frac{v}{a}\frac{\partial}{\partial\varphi}().$$

Following McDonald and Bates (1989), we include the divergence damping in the equations for numerical stability, and the damping coefficient is generally set as 6.8×10^6 m^2 s^{-1} unless it is specified otherwise. Here N_u and N_v are the spherical metric terms (i.e., the curvature term) given by

$$N_u = \frac{uv\tan\varphi}{a} \quad \text{and} \quad N_v = -\frac{u^2\tan\varphi}{a}.$$

Here we denote h_w as the depth of fluid and h is the total height of the free surface. In case the effect of the topography $h_s(\lambda, \varphi)$ is included, the total height of the water surface is $h = h_w + h_s$.

The conservative form of the shallow-water equations in longitude–latitude grid is represented (Rossmanith et al. 2004; Rossmanith 2006) as

$$\frac{\partial}{\partial t}\left(\sqrt{G}h_w\right) + \frac{\partial(ah_w u)}{\partial\lambda} + \frac{\partial(a\cos\varphi h_w v)}{\partial\varphi} = 0, \quad (17)$$

$$\frac{\partial}{\partial t}(\sqrt{G}h_w u^1) + \frac{\partial\left[\left(h_w u^2 + \frac{1}{2}gh_w^2\right)/\cos\varphi\right]}{\partial\lambda} + \frac{\partial(h_w uv)}{\partial\varphi} = (fa + 2u\tan\varphi)h_w v - gh_w\frac{1}{\cos\varphi}\frac{\partial h_s}{\partial\lambda}, \quad \text{and} \quad (18)$$

$$\frac{\partial(\sqrt{G}h_w u^2)}{\partial t} + \frac{\partial(h_w uv)}{\partial\lambda} + \frac{\partial\left[\cos\varphi\left(h_w v^2 + \frac{1}{2}gh_w^2\right)\right]}{\partial\varphi} = -(fa\cos\varphi + u\sin\varphi)h_w u - \frac{1}{2}gh_w^2\sin\varphi - gh_w\cos\varphi\frac{\partial h_s}{\partial\varphi}, \quad (19)$$

where $\sqrt{G}h_w$, $\sqrt{G}h_w u^1$, and $\sqrt{G}h_w u^2$ are the conservative variables whose VIA values are updated by flux-based finite-volume formulations given later. The contravariant velocity components are $u^1 = (u/a\cos\varphi)$ and $u^2 = (v/a)$ with the metric factor being $\sqrt{G} = a^2\cos\varphi$.

b. The semi-implicit semi-Lagrangian procedure for PVs

Since the pioneering work of Wiin-Nielsen (1959), the semi-Lagrangian scheme has received much attention for its superiority in computational stability and efficiency for large time steps. Robert (1981, 1982) has obtained stable integrations for the shallow-water equations of different forms with large time steps, using a semi-Lagrangian semi-implicit model. Since then, many researchers such as Ritchie (1985) and McDonald and Bates (1987, 1989) have investigated the numerical accuracy, computational stability, and efficiency of the semi-implicit semi-Lagrangian scheme. Staniforth and Côté (1991) gave a detailed review of this method and its applications to numerical models for atmospheric dynamics. In the present paper, we use the semi-implicit semi-Lagrangian solution to update the PVs.

Following the procedure used by McDonald and Bates (1989), we integrate the momentum equations [Eqs. (14) and (15)] in two half time steps of $\Delta t/2$. In the first half-step (i.e., the semi-Lagrangian step) the Coriolis terms are treated implicitly while the pressure gradient and the divergence damping terms are treated explicitly. The reason is that we can easily solve the half-time-level momentum directly by ways of semi-Lagrangian method, so it is called the semi-Lagrangian step. The second half-step, which is called the semi-implicit step, starts with those terms obtained from the first half-step. The curvature terms are integrated for a single time step Δt in the first step. The continuity equation [Eq. (16)] is integrated in a full step of Δt.

Let $\bar{h}$ be a constant reference height such that $h = \bar{h} + h'$ and $|h'| \ll \bar{h}$. In the all test cases presented in this paper, we set $\bar{h}$ as h_0 in the initial condition for height. Sorting all the $(n+1)$th time-level quantities to the left-hand side in the resulting equations we have

$$\left[u + \frac{\Delta t}{2}\frac{1}{a\cos\varphi}\frac{\partial}{\partial\lambda}(gh - cD)\right]^{n+1} = B_u, \tag{20}$$

$$\left[v + \frac{\Delta t}{2}\frac{1}{a}\frac{\partial}{\partial\varphi}(gh - cD)\right]^{n+1} = B_v, \tag{21}$$

and

$$\left[h_w + \frac{\Delta t}{2}\bar{h}D\right]^{n+1} = B_h, \tag{22}$$

where

$$B_u = [(W_u)^n + \mathcal{F}(W_v)^n]_d,$$
$$B_v = [(W_v)^n + \mathcal{F}(W_u)^n]_d, \quad \text{and}$$
$$B_h = \left[(h_w)^n - \left(\frac{\Delta t}{2}\bar{h} + \Delta t h'\right)^n\right]_d,$$

with

$$W_u = \frac{Y_u + \mathcal{F}Y_v}{1 + \mathcal{F}^2},$$
$$W_v = \frac{Y_v + \mathcal{F}Y_u}{1 + \mathcal{F}^2},$$
$$Y_u = u - \frac{\Delta t}{2}\frac{1}{a\cos\varphi}\frac{\partial}{\partial\lambda}(gh - cD) + \Delta t N_u,$$
$$Y_v = v - \frac{\Delta t}{2}\frac{1}{a}\frac{\partial}{\partial\varphi}(gh - cD) + \Delta t N_v, \quad \text{and}$$
$$\mathcal{F} = f\frac{\Delta t}{2}.$$

In the above expressions, the subscript "d" denotes the position at the departure point where the corresponding value of the physical field should be obtained from the multimoment reconstruction described in section 3.

From Eqs. (20) and (21) we find

$$D^{n+1} = \nabla\cdot\mathbf{B} - \frac{\Delta t}{2}\nabla^2(gh - cD)^{n+1}, \tag{23}$$

where $\mathbf{B} = (B_u, B_v)$. Eliminating D^{n+1} between Eqs. (22) and (23) leads to the Helmholtz equation

$$\nabla^2 h_w^{n+1} - \mu^2 h_w^{n+1} = H, \tag{24}$$

where

$$\mu^2 = \left[\left(\frac{\Delta t}{2}\right)^2 g\bar{h} + c\frac{\Delta t}{2}\right]^{-1}$$

and

$$H = \mu^2\left[\left(\frac{\Delta t}{2}\bar{h}\right)\nabla\cdot\mathbf{B} + \left(c\frac{\Delta t}{2}\nabla^2 - 1\right)B_h - \left(\frac{\Delta t}{2}\right)^2\bar{h}\nabla^2(gh_s)\right].$$

The spatial discretization for above semi-implicit semi-Lagrangian formulation is carried out completely in terms of the PVs. The great circle algorithm of McDonald and Bates (1989) is used to determine the departure location and the detailed procedures can be found in Li et al. (2006). For the eight PV moments (black circle) shown in Fig. 2, we can directly utilize the interpolation function $F_{i,j}(\lambda, \varphi)$ constructed in the previous section to obtain the velocity components u, v,

and the height h field at the departure point. For the value at the triangle point $\overline{{}^{P}\Phi}^{n}_{i,j}$ in Fig. 2, which is not a model variable, we should evaluate its value at the departure point by using the same interpolation function $F_{i,j}$ (λ, φ) since we will need it in the semi-implicit semi-Lagrangian solution. For the pressure gradient term, we first utilize central differencing to evaluate the gradient in the arrival point at the current time level, then use a third-order Lagrangian interpolation function (Li et al. 2006) based on 16 grid points to obtain the gradient value at the departure point. At this step, the point value at the cell center is involved as other PVs and should be computed from the multimoment reconstruction. We have then obtained the right-hand side terms in the prognostic equations [Eqs. (20)–(22)]. With all the values at the departure points known, we can obtain the right-hand side of the Helmhotlz equation H in Eq. (24).

The Laplacian operator in Eq. (24) in a longitude–latitude grid is

$$\nabla^2() = \frac{1}{a^2\cos^2\varphi}\frac{\partial^2()}{\partial\lambda^2} + \frac{1}{a^2\cos\varphi}\frac{\partial}{\partial\varphi}\left[\frac{\cos\varphi\partial()}{\partial\varphi}\right]. \quad (25)$$

Shown in Fig. 3, a five-point central differencing in terms of $\overline{{}^{P}\Phi}^{n}_{i-1,j}$, $\overline{{}^{P}\Phi}^{n}_{i,j}$, $\overline{{}^{P}\Phi}^{n}_{i+1,j}$, $\overline{{}^{P}\Phi}^{n}_{i,j-1}$, and $\overline{{}^{P}\Phi}^{n}_{i,j+1}$ is used to approximate the second derivative at the (i, j) point. Because of the uniform spacing in respect to λ and φ, we have

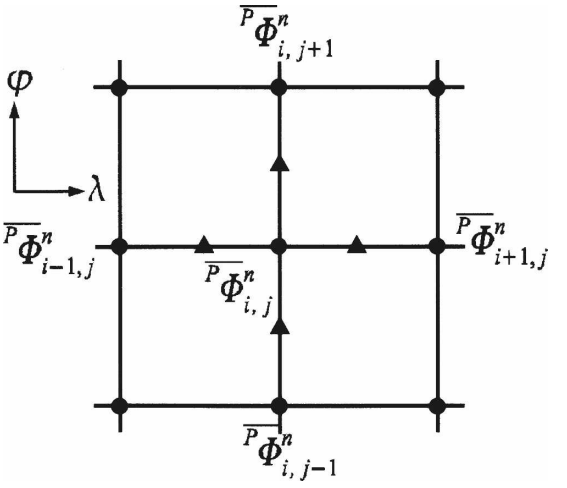

FIG. 3. The mesh diagram for discretizing the Helmholtz equation. The PV of the water height is directly solved from the Helmholtz equation and then used in evaluating the gradient forces for the neighboring PVs. The triangle marks denote the central points where the trigonometric function in Eq. (27) must be calculated in the φ direction.

$$\left(\frac{\partial^2\Phi}{\partial\lambda^2}\right)_{i,j} = \frac{\overline{{}^{P}\Phi}_{i+1,j} + \overline{{}^{P}\Phi}_{i-1,j} - 2\overline{{}^{P}\Phi}_{i,j}}{\Delta\lambda^2} \quad \text{and} \quad (26)$$

$$\left[\frac{\partial}{\partial\varphi}\left(\frac{\cos\varphi\partial(\Phi)}{\partial\varphi}\right)\right]_{i,j} = \frac{\cos\varphi_{i,j+1/2}\dfrac{\overline{{}^{P}\Phi}_{i,j+1} - \overline{{}^{P}\Phi}_{i,j}}{\Delta\varphi} - \cos_{i,j-1/2}\dfrac{\overline{{}^{P}\Phi}_{i,j} - \overline{{}^{P}\Phi}_{i,j-1}}{\Delta\varphi}}{\Delta\varphi}. \quad (27)$$

Note that the trigonometric functions $\cos\varphi_{i,j+1/2}$ and $\cos\varphi_{i,j-1/2}$ are computed at the middle points shown as the triangle marks in the φ direction in Fig. 3.

The discretized Helmholtz equation has to be solved over the whole sphere for a globally converged numerical solution. Extra attention must be paid in the overlapping region of the Yin–Yang grid. As shown in Fig. 4, when we discretize the Helmholtz equation at a boundary point N in the Yang component, for example, the value of Φ at point M that falls in the Yin component (indicated by the dashed lines) is needed. The value of Φ out of the boundary (the solid line) is interpolated by a third-order Lagrangian interpolation function (Li et al. 2006) based on the 16 points from another component grid (Yin grid). The same applies when Helmholtz equation is solved on the Yin grid and requires the value at a point falling in the Yang grid.

The Helmholtz equation is solved iteratively by the classical Schwarz method on the Yin–Yang grid with the boundary data exchanged at every step through the interpolation. Thus, the equivalent overlap subdomain in context of the Schwarz method is "one". In our computations, we require the residual for both the Yin and Yang grids to be less than 10^{-8}. It is noted that Qaddouri et al. (2007) recently introduced an optimized Schwarz methods in the Yin–Yang grid by using improved transmission conditions across the Yin–Yang boundary.

Successive overrelaxation (SOR; Press et al. 1992) is used to solve the Helmholtz equation on each component of the Yin–Yang grid, respectively, in the present model. As expected, the iteration number needed for convergence depends on the problem size. Shown in Table 1, more iteration number is required for simulation with higher resolution. Other more scalable solver, such as the multigrid methods (Wesseling 1991) should

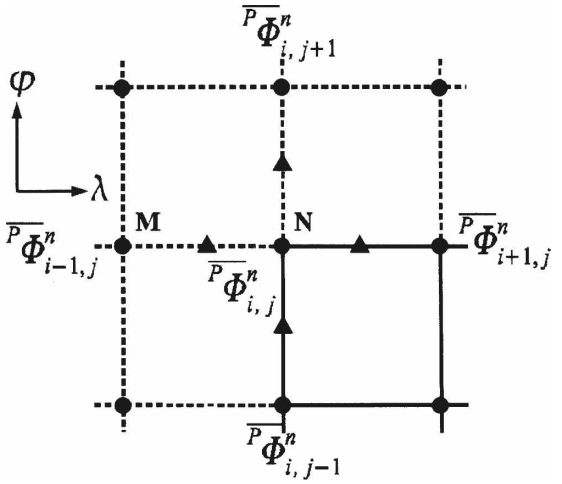

FIG. 4. Spatial discretization of the Helmholtz equation in the CIP/MM FVM grid. The triangle marks denote the central difference points for solving the Helmholtz equation.

be more demanding in large-scale simulation. We summarize the procedure for getting numerical solution to the Helmholtz equation [Eq. (24)] on the Yin–Yang grid as follows:

1) Calculate the values at the boundary points (e.g., point M in Fig. 4) of the Yang grid from the Yin grid by interpolation.
2) Use SOR iterative method to solve the Helmholtz equation in the Yang component to update the numerical solution of the Helmholtz equation for one step.

TABLE 1. Iteration numbers needed for the numerical solution of the Helmholtz equation to converge (with the maximum residual on both the Yin and Yang grids being less than 10^{-8}). Displayed are the numbers on Yin grid/the numbers on Yang grid.

Resolution	Case 2	Case 5	Case 6	Case 7
$16 \times 48 \times 2$	10/11	13/13	14/15	15/15
$32 \times 96 \times 2$	17/19	26/26	30/31	31/32
$64 \times 192 \times 2$	38/43	72/69	84/87	88/92

3) Interpolate the values at the boundary points for the Yin grid from the Yang grid by interpolation in a similar manner.
4) Similar to step 2, iterate the Helmholtz equation in the Yin component grid to update the numerical solution for one step.
5) Repeat steps 1–4 until the numerical solution converges on both the Yin and Yang grids.

Once we get the water height field h_w^{n+1} as the solution of the Helmholtz equation at the next time level, we can evaluate the velocity components u^{n+1} and v^{n+1} at the next time level by Eqs. (20) and (21).

c. *The flux-based finite-volume method for VIA*

As mentioned before, the VIA moment is updated in terms of the flux form shallow-water equation system in Eqs. (17)–(19). We recast them into a vector form as

$$\frac{\partial \mathbf{U}}{\partial t} = -\frac{\partial \mathbf{F}(\mathbf{U})}{\partial \lambda} - \frac{\partial \mathbf{G}(\mathbf{U})}{\partial \varphi} + \mathbf{S}(\mathbf{U}), \tag{28}$$

where

$$\mathbf{U} = \begin{bmatrix} a^2 \cos\varphi h_w \\ a h_w u \\ a \cos\varphi h_w v \end{bmatrix}, \quad \mathbf{F}(\mathbf{U}) = \begin{bmatrix} a h_w u \\ \left(h_w u^2 + \frac{1}{2} g h_w^2 / \cos\varphi \right) \\ h_w u v \end{bmatrix}, \quad \mathbf{G}(\mathbf{U}) = \begin{bmatrix} a \cos\varphi h_w v \\ h_w u v \\ \cos\varphi \left(h_w v^2 + \frac{1}{2} g h_w^2 \right) \end{bmatrix}, \quad \text{and}$$

$$\mathbf{S}(\mathbf{U}) = \begin{bmatrix} 0 \\ (fa + 2u \tan\varphi) h_w v - g h_w \dfrac{1}{\cos\varphi} \dfrac{\partial h_s}{\partial \lambda} \\ -(fa \cos\varphi + u \sin\varphi) h_w u - \dfrac{1}{2} g h_w^2 \sin\varphi - g h_w \cos\varphi \dfrac{\partial h_s}{\partial \varphi} \end{bmatrix}.$$

We have the VIA within the domain $\Omega_{i,j}$ as

$$\overline{{}^{V}\mathbf{U}}_{i,j} = \frac{1}{\Delta\lambda_i \Delta\varphi_j} \int_{\lambda_{i-1/2}}^{\lambda_{i+1/2}} \int_{\varphi_{j-1/2}}^{\varphi_{j+1/2}} \mathbf{U}(\lambda, \varphi, t)\, d\lambda\, d\varphi\,. \tag{29}$$

The governing equations for VIA are obtained by integrating Eq. (28) over domain $\Omega_{i,j}$:

$$\frac{\partial \overline{{}^{V}\mathbf{U}}_{i,j}}{\partial t} = -\frac{1}{\Delta\lambda_i \Delta\varphi_j}\left\langle \left\{ \int_{\varphi_{j-1/2}}^{\varphi_{j+1/2}} [\mathbf{F}(\mathbf{U})_{i+1/2} - \mathbf{F}(\mathbf{U})_{i-1/2}]\, d\varphi + \int_{\lambda_{i-1/2}}^{\lambda_{i+1/2}} [\mathbf{G}(\mathbf{U})_{j+1/2} - \mathbf{G}(\mathbf{U})_{j-1/2}]\, d\lambda \right\} \right\rangle$$
$$+ \frac{1}{\Delta\lambda_i \Delta\varphi_j} \int_{\lambda_{i-1/2}}^{\lambda_{i+1/2}} \int_{\varphi_{j-1/2}}^{\varphi_{j+1/2}} \mathbf{S}(\mathbf{U})\, d\lambda\, d\varphi \equiv \mathcal{L}(\mathbf{U})_{i,j}. \tag{30}$$

Given all the PVs on the control volume boundary, the integrals over the boundary segments in Eq. (30) are computed by the three-point quadrature formula:

$$\int_{\varphi_{j-1/2}}^{\varphi_{j+1/2}} \mathbf{F}(\mathbf{U})_{i+1/2}\, d\varphi \approx \frac{\Delta\varphi_j}{6} [\mathbf{F}(\overline{{}^{P}\mathbf{U}})_{i-1/2,j-1/2} + 4\mathbf{F}(\overline{{}^{P}\mathbf{U}})_{i-1/2,j} + \mathbf{F}(\overline{{}^{P}\mathbf{U}})_{i-1/2,j+1/2}].$$

The area integral of source term is computed by the following nine-point quadrature formula:

$$\int_{\lambda_{i-1/2}}^{\lambda_{i+1/2}} \int_{\varphi_{j-1/2}}^{\varphi_{j+1/2}} \mathbf{S}(\mathbf{U})\, d\lambda\, d\varphi \approx \Delta\lambda_i \Delta\varphi_j \left\{ \frac{1}{36} [\mathbf{S}(\overline{{}^{P}\mathbf{U}})_{i-1/2,j-1/2} + \mathbf{S}(\overline{{}^{P}\mathbf{U}})_{i+1/2,j-1/2} + \mathbf{S}(\overline{{}^{P}\mathbf{U}})_{i-1/2,j+1/2} + \mathbf{S}(\overline{{}^{P}\mathbf{U}})_{i+1/2,j+1/2}] \right.$$
$$\left. + \frac{1}{9} [\mathbf{S}(\overline{{}^{P}\mathbf{U}})_{i-1/2,j} + \mathbf{S}(\overline{{}^{P}\mathbf{U}})_{i+1/2,j} + \mathbf{S}(\overline{{}^{P}\mathbf{U}})_{i,j-1/2} + \mathbf{S}(\overline{{}^{P}\mathbf{U}})_{i,j+1/2}] + \frac{4}{9} \mathbf{S}(\overline{{}^{P}\mathbf{U}})_{i,j} \right\}.$$

Since the PVs at step $n + 1$ are already known from the semi-implicit semi-Lagrangian procedure discussed above, a second-order time integration can be used for VIA as

$$\overline{{}^{V}\mathbf{U}}^{n+1} = \overline{{}^{V}\mathbf{U}}^{n} + \frac{\Delta t}{2} [\mathcal{L}(\mathbf{U})_{i,j}^{n+1} + \mathcal{L}(\mathbf{U})_{i,j}^{n}], \tag{31}$$

where $\mathcal{L}(\mathbf{U})_{i,j}^{n}$ and $\mathcal{L}(\mathbf{U})_{i,j}^{n+1}$ means the right-hand sides of Eq. (30) computed with the PVs at the nth and the $(n + 1)$th step, respectively.

Because we have to keep both PV and VIA independently as the model variables, the present model requires twice as much as the memory storage needed in a single-moment model. Relative to the conventional semi-Lagrangian/semi-implicit scheme, extra computation cost is required for the numerical fluxes in Eq. (30). Given the PV moments that are updated at an expense, which is almost the same as in a conventional semi-Lagrangian scheme, the numerical fluxes can be explicitly computed. In Table 2, we show the CPU time consumed by different parts of the model for different resolutions. Updating VIA takes only a small portion of the total CPU time.

As discussed above, adding a conserved moment (i.e., the volume integrated value) provides us a convenient way to enforce the numerical conservativeness in a semi-Lagrangian semi-implicit model. Being a general methodology, it should be able to apply to other semi-Lagrangian semi-implicit formulations as well. As another particular way to introduce the conservation to a semi-Lagrangian semi-implicit model, we note that Lauritzen et al. (2006) presented a mass-conservative semi-Lagrangian semi-implicit model by using a volume-mapping advection transport scheme.

5. The advection scheme

For completeness, we briefly describe the advection scheme used in the numerical tests in this paper.

The two-dimensional flux-form advection equation for any scalar h can be expressed as

$$\frac{\partial h}{\partial t} + \frac{\partial}{\partial \lambda}(\tilde{u}h) + \frac{\partial}{\partial \mu}(\tilde{v}h) = 0 \tag{32}$$

on the sphere, where

$$\tilde{u} = \frac{u\cos\varphi}{a(1-\mu^2)}, \quad \tilde{v} = \frac{v\cos\varphi}{a}, \quad \text{and} \quad \mu = \sin\varphi.$$

As discussed above, both the VIA and PV as the model variables need to be predicted in time.

We update the PV moment by a semi-Lagrangian scheme, considering the advection form of Eq. (32):

$$\frac{dh}{dt} = -D,$$

where D denotes the divergence as given before.

With the interpolation function in Eq. (13) constructed in terms of both PV and VIA moments at time step n, one can predict the PVs on the cell boundary by

$$\overline{{}^{P}h}^{n+1}(\lambda_\zeta, \varphi_\vartheta) = F_{\text{up}}(\lambda_\zeta - \delta\lambda_\zeta, \varphi_\vartheta - \delta\varphi_\vartheta) - \int_C D\, dt, \tag{33}$$

where subscript "up" denotes the piecewise interpolation function for the cell in which the departure point $(\lambda_\zeta - \delta\lambda_\zeta, \varphi_\vartheta - \delta\varphi_\vartheta)$ falls, and C is the trajectory connecting the departure and arrival points. The displacement $(\delta\lambda_\zeta, \delta\varphi_\vartheta)$ is computed according to the velocity field. In the present model the great circle algorithm of

TABLE 2. Elapsed time in seconds per step. The hardware platform is a single node (single CPU of 1.9 GHz, 8 GB memory) of an IBM cluster1600 (AIX, version 5). "Helmholtz Eq.," "PV," "VIA," "Other," and "Tot" denote the time for solving Helmholtz equation, updating PV moments (including the computation of Helmholtz equation), updating the VIA moment, the other part, and the total time per step, respectively.

Resolution	Helmholtz Eq.	PV	VIA	Other	Tot
$16 \times 48 \times 2$	0.11	0.18	0.01	0.05	0.24
$32 \times 96 \times 2$	0.34	0.59	0.01	0.15	0.75
$64 \times 192 \times 2$	1.17	2.14	0.04	0.50	2.68

McDonald and Bates (1989) is used to determine the departure location.

Given all the PVs for both the nth and $(n + 1)$th time steps on the control volume boundary, the VIA moment of the advected field $\overline{V}h_{i,j}^{n+1}$ can be computed by a finite-volume formulation in the same exact way as the first equation of Eq. (30).

The interpolation for communicating data across the Yin–Yang boundary in the advection computations is conducted in the same manner as previously discussed.

TABLE 3. Normalized errors of the cosine bell advection test with different orientation angles.

Resolution	ℓ_1	ℓ_2	ℓ_∞
$\alpha = 0$	4.52×10^{-2}	3.09×10^{-2}	2.76×10^{-2}
$\alpha = \pi/4$	5.31×10^{-2}	3.19×10^{-2}	2.05×10^{-2}
$\alpha = \pi/2$	4.91×10^{-2}	3.17×10^{-2}	2.63×10^{-2}

6. Numerical tests

According to Williamson et al. (1992), we define the global integral I as

$$I(h) = \frac{1}{4\pi}\int_{\pi/4}^{7\pi/4}\int_{\pi/4}^{-\pi/4} h_{\text{yin}}(\lambda, \varphi)\cos\varphi \, d\varphi \, d\lambda + \frac{1}{4\pi}\int_{\pi/4}^{7\pi/4}\int_{\pi/4}^{-\pi/4} h_{\text{yang}}(\lambda, \varphi)\cos\varphi \, d\varphi \, d\lambda, \tag{34}$$

and the normalized global errors as

$$\ell_1(h) = \frac{I[|h(\lambda, \varphi) - h_T(\lambda, \varphi)|]}{I[|h_T(\lambda, \varphi)|]}, \tag{35}$$

$$\ell_2(h) = \frac{\langle I\{[h(\lambda, \varphi) - h_T(\lambda, \varphi)]^2\}\rangle^{1/2}}{I\{[h_T(\lambda, \varphi)]^2\}^{1/2}}, \quad \text{and} \tag{36}$$

$$\ell_\infty(h) = \frac{\max[|h_{\text{yang}}(\lambda, \varphi) - h_{\text{yang},T}(\lambda, \varphi)|, |h_{\text{yin}}(\lambda, \varphi) - h_{\text{yin},T}(\lambda, \varphi)|]}{\max[|h_{\text{yang},T}(\lambda, \varphi)|, |h_{\text{yin},T}(\lambda, \varphi)|]}, \tag{37}$$

where $h_{\text{yang},T}(\lambda, \varphi)$ and $h_{\text{yin},T}(\lambda, \varphi)$ are the true solutions on the Yin–Yang grids, respectively. Note that Eq. (34) indicates that the integral over the overset region of the Yin–Yang grid is computed twice.

a. Solid-body rotation of a cosine bell

The cosine bell advection test proposed by Williamson et al. (1992) is often employed to test global advection schemes. The initial distribution of the transported tracer is given by

$$h(\lambda, \varphi) = \begin{cases} 0.5[1 + \cos(\pi r/R)], & \text{if} \quad r < R = a/3, \\ 0, & \text{if} \quad r \geq R = a/3, \end{cases} \tag{38}$$

where $r = a\cos^{-1}[\sin\varphi_0 \sin\varphi + \cos\varphi_0 \cos\varphi \cos(\lambda - \lambda_0)]$, and the center of the distribution is $\lambda_0 = \pi/2$ and $\varphi_0 = 0$.

The wind components are

$$u = u_0(\cos\varphi \cos\alpha + \sin\varphi \cos\lambda \sin\alpha) \quad \text{and} \tag{39}$$

$$v = -u_0 \sin\lambda \sin\varphi, \tag{40}$$

where the parameter α is the angle between the axis of the solid-body rotation and the polar axis of the spherical coordinate system. Tests in this paper were run with $\alpha = 0$, $\alpha = \pi/4$, $\alpha = \pi/2$, and $u_0 = 2\pi a/(12 \text{ days})$.

We carried out global advection tests with the resolution of $2.8125° \times 2.8125°$ (equivalent to a $32 \times 96 \times 2$ grid). The Courant–Friedrichs–Lewy (CFL) number is specified as 0.5. The normalized errors are shown in Tables 3 for different angles. It reveals that the Yin–Yang grid can get accurate advections along different paths on the sphere. The transported concentration and difference between the numerical solution and exact solution are shown in Fig. 5 for $\alpha = \pi/4$. The time evolution of the corresponding ℓ_1, ℓ_2, and ℓ_∞ errors for $\alpha = \pi/4$ and $\alpha = \pi/2$ are also given in Fig. 5.

We compared our numerical results with other existing global advection schemes. For the convenience of intercomparison, we referenced the numerical results from other schemes, such as the semi-Lagrangian trans-

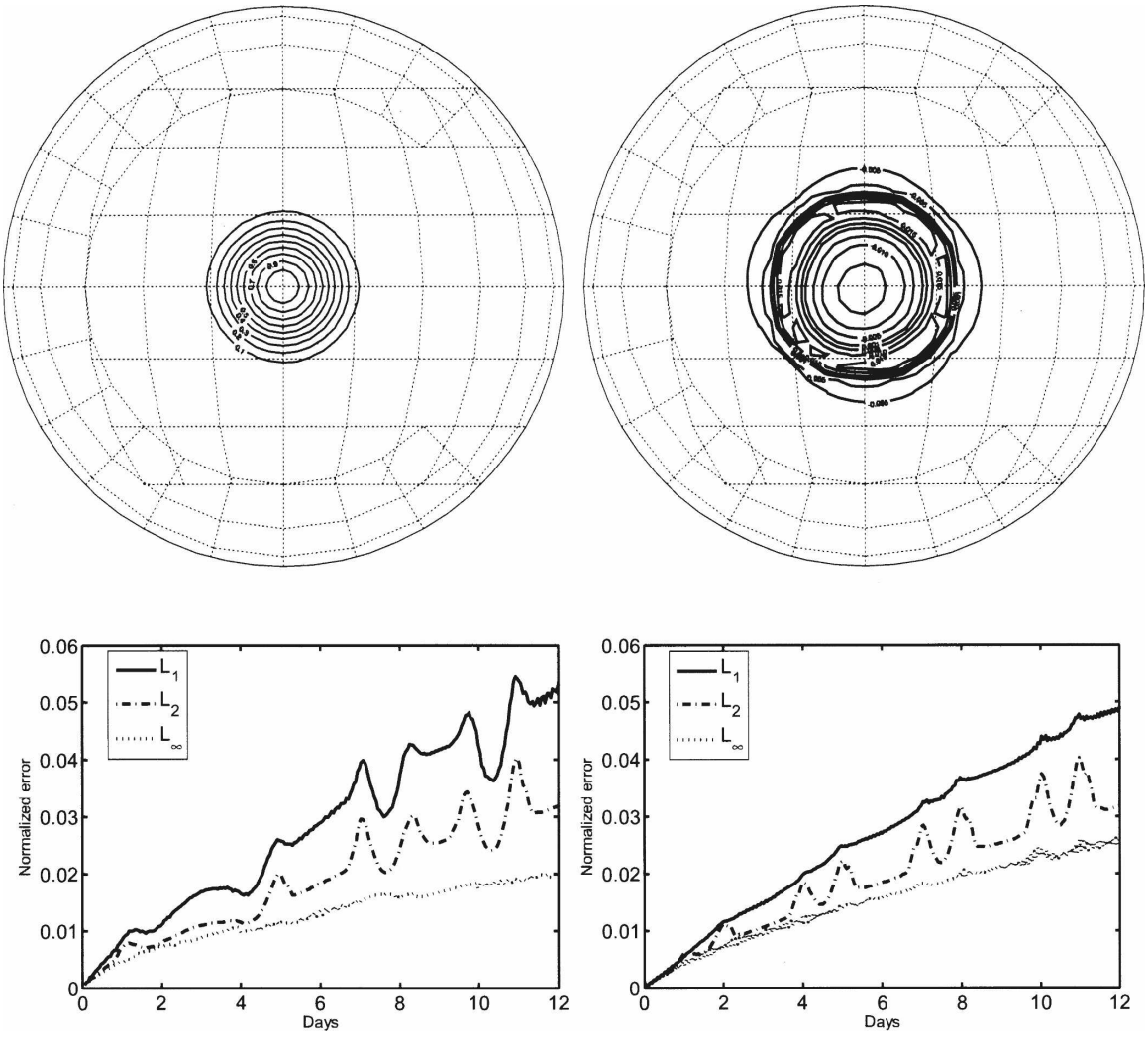

FIG. 5. Advection of a cosine hill after one revolution around the globe (CFL = 0.5). (top left) The numerical solution and (top right) the difference between the numerical solution and the true solution for $\alpha = \pi/4$. The contour of the top-left panel is from 0.1 to 0.9 and that of the top-right panel is from −0.015 to 0.015. (bottom) The time evolution of ℓ_1, ℓ_2, and ℓ_∞ errors for (left) $\alpha = \pi/4$ and (right) $\alpha = \pi/2$ are plotted separately. A $32 \times 96 \times 2$ grid is used in the test.

port on a reduced grid (RG; see Table 2 of Rasch 1994), the conservative cell-integrated semi-Lagrangian scheme (CISL; see Table 1 of Nair and Machenhauer 2002), flux-form semi-Lagrangian (FFSL; see Table 6 of Lin and Rood 1996), the semi-Lagrangian inherently conserving and efficient scheme (SLICE; see Table 1 of Zerroukat et al. 2004), and the constrained interpolation profile/conservative semi-Lagrangian scheme with rational function (CIP-CSLR; see Table 3 of Peng et al. 2006). In Table 4, the maximum and minimum norms are defined as in Rasch (1994), and YY-MM denotes our multimoment scheme in the Yin–Yang grid. YY-L and YY-C, RG2.8 and RG2.8-M, FFSL-3 and FFSL-5, CISL-M and CISL-P, and SLICE-S stand for the corresponding schemes in Peng et al. (2006), Rasch (1994),

TABLE 4. Error measures for the solid-body rotation of a cosine bell after one revolution (256 steps). For comparison, results of other existing global advection schemes are also presented. See the text for details.

Scheme	ℓ_1	ℓ_2	ℓ_∞	Max	Min
YY-MM	0.049	0.032	0.026	−0.014	−0.013
YY-L	—	0.091	0.108	−0.091	−0.002
YY-C	—	0.060	0.092	−0.090	−0.002
RG2.8	0.289	0.176	0.164	−0.150	−0.027
RG2.8M	0.181	0.158	0.196	−0.210	0
FFSL-3	0.078	0.079	0.124	−0.124	−0.001
FFSL-5	0.047	0.041	0.053	−0.053	−0.001
CISL-M	0.084	0.084	0.109	−0.052	0
CISL-P	0.059	0.045	0.048	−0.016	−0.003
SLICE-S	0.079	0.049	0.042	—	—

TABLE 5. Normalized errors and convergence rates of smooth wave advection in the Yin–Yang grid. CFL = 0.5, and $\alpha = 0$.

Resolution	ℓ_1	ℓ_1 order	ℓ_2	ℓ_2 order	ℓ_∞	ℓ_∞ order
$16 \times 48 \times 2$	4.99×10^{-4}	—	5.13×10^{-4}	—	8.01×10^{-4}	—
$32 \times 96 \times 2$	6.22×10^{-5}	3.00	6.52×10^{-5}	2.98	1.07×10^{-4}	2.90
$64 \times 192 \times 2$	7.73×10^{-6}	3.01	8.18×10^{-6}	2.99	1.40×10^{-5}	2.93

Lin and Rood (1996), Nair and Machenhauer (2002), and Zerroukat et al. (2004), respectively. The error measures show that the multimoment finite-volume scheme on Yin–Yang grid (YY-MM) has a competitive numerical accuracy.

b. *Advection test of a sine wave*

A more smooth distribution of a sine wave (Li et al. 2006) was used to evaluate the convergence rate of the scheme with grid refinement. In this test, we choose the CFL equal to be 0.5.

The initial condition is defined by

$$h(\lambda, \varphi) = h_0 \cos^4\varphi \sin(k\lambda), \tag{41}$$

where $h_0 = 1$ and $k = 4$ is the wavenumber. The velocity component fields are the same as those of solid-body rotation of a cosine bell.

In this test, three levels of grids with the grid spacing

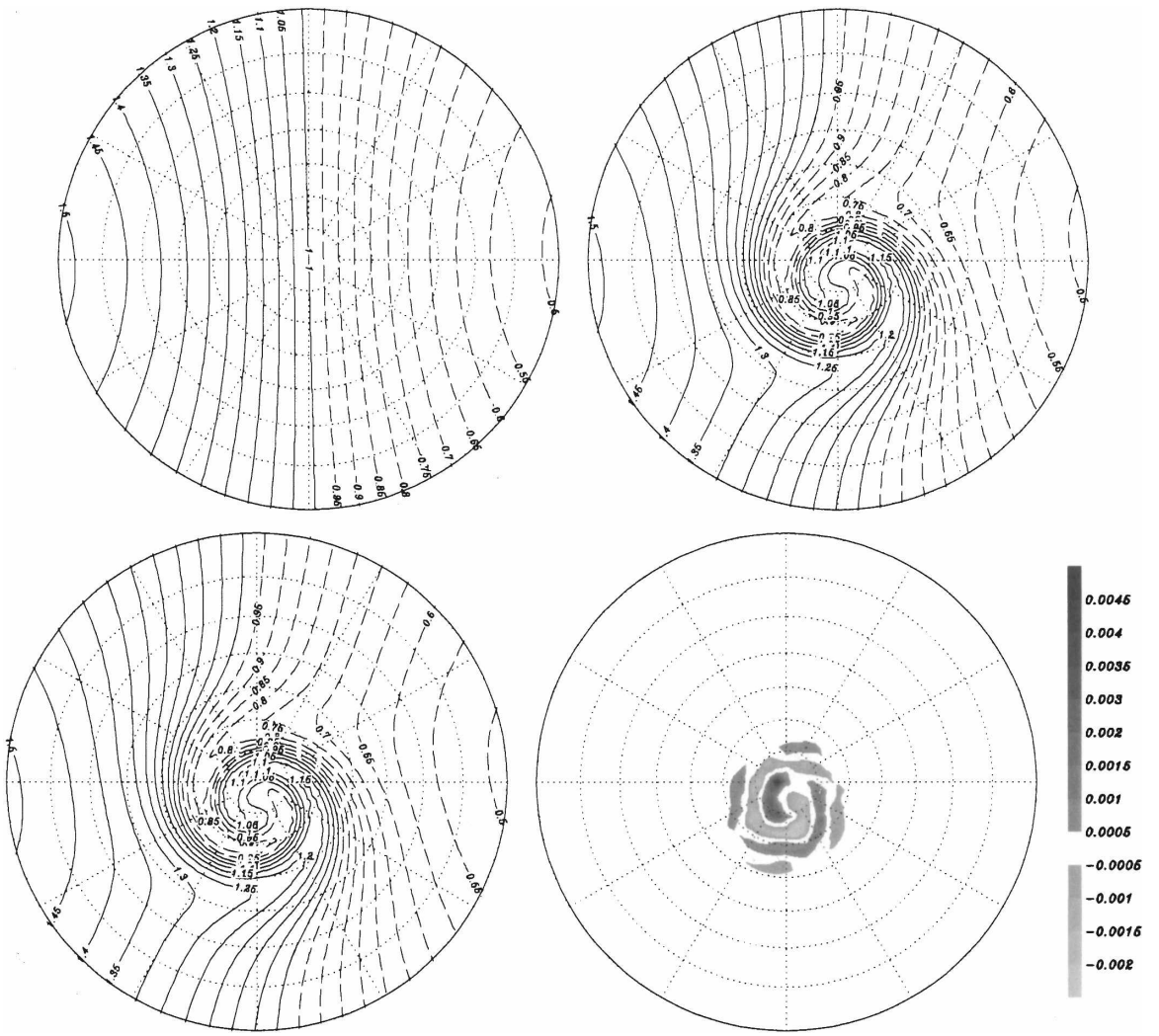

FIG. 6. Results of the polar vortex test: (top left) the initial condition, (top right) the analytical solution at $t = 3$, (bottom left) the numerical solution, and (bottom right) the difference between the analytical and numerical solutions at $t = 3$. A $32 \times 96 \times 2$ computational grid is used in the simulation.

TABLE 6. Comparison of normalized errors at different times for the cyclogenesis test. A $32 \times 96 \times 2$ grid is used. The results at $t = 3$ (after 32 time steps) and $t = 6$ (after 64 time steps) are given. For comparison, we include the numerical results of other existing schemes as well.

	YY-MM		SLICES-S		BiCubic-SL		CISL-P		CISL-M	
t	3	6	3	6	3	6	3	6	3	6
ℓ_1	0.000 07	0.000 77	0.000 86	0.003 44	0.000 48	0.004 06	0.001 10	—	0.001 30	—
ℓ_2	0.000 22	0.002 07	0.002 56	0.011 47	0.001 83	0.014 23	0.002 50	—	0.003 10	—
ℓ_∞	0.004 21	0.015 53	0.015 53	0.080 26	0.011 07	0.072 85	0.014 40	—	0.021 10	—

gradually refined were used. As shown in Table 5, a third-order accuracy is verified on the Yin–Yang grid.

c. Cyclogenesis test

A more severe experiment was performed using the deformational vortex flow (Peng et al. 2006; Nair et al. 1999, 2005b; Nair and Machenhauer 2002; Zerroukat et al. 2004) on a rotated spherical coordinate (λ', φ') with the rotated north pole at $(\pi + 0.025, \pi/2.2)$. The vortical velocity field is specified as

$$V_t = \frac{3\sqrt{3}}{2} \tanh(r') \operatorname{sech}^2(r'), \tag{42}$$

where $r' = r_0 \cos\varphi'$ is the radial distance to the center of the vortex and $r_0 = 3$. The angular velocity is defined to be

$$\omega'(\varphi') = \begin{cases} V_t/r', & \text{if} \quad r' \neq 0, \\ 0, & \text{if} \quad r' = 0. \end{cases} \tag{43}$$

The analytical solution is

$$q(\lambda', \varphi', t) = 1 - \tanh\left[\frac{r'}{d} \sin(\lambda' - \omega' t)\right], \tag{44}$$

where $d = 5$ and the initial state is given as $t = 0$ in Eq. (44).

In this test, $32 \times 96 \times 2$ cells are employed in the computation. The numerical result after 32 time steps is given with the corresponding analytical one in Fig. 6. The structure of the vortex center is well captured by our scheme and is in good agreement with the analytical one. Table 6 shows the numerical errors of the CIP/MM FVM as well as other existing schemes, such as SLICE-S (see Table 3 of Zerroukat et al. 2004), CISL (see Table 4 of Nair and Machenhauer 2002), and the standard nonconservative bicubic semi-Lagrangian scheme (BiCubic-SL). Again, our multimoment scheme is found to be competitive.

d. Geostrophic flow across the Pole

This test is proposed by McDonald and Bates (1989), simulating a cross-polar flow with a geostrophically balanced initial state.

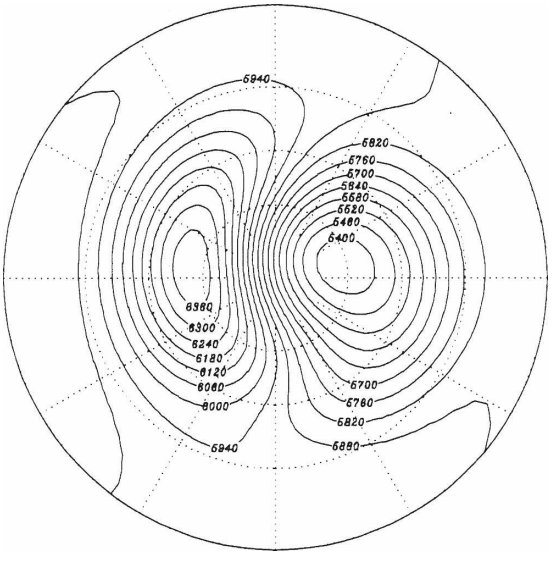

FIG. 7. The numerical solution at day 5 with $\Delta\lambda = \Delta\varphi = 2.8125°$, $c = 6.8 \times 10^6$ m^2 s^{-1}, and $\Delta t = 600$ s. The contour interval is 60 m.

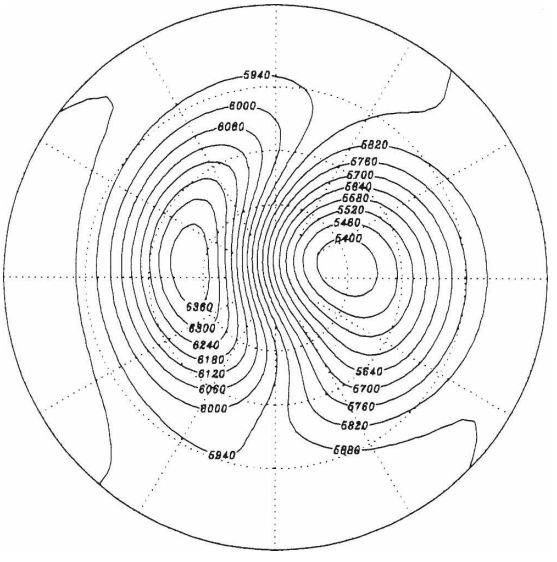

FIG. 8. As in Fig. 7, but with $\Delta t = 1800$ s.

The initial height and velocity components are given by

$$gh = gh_0 + 2\Omega a v_0 \sin^3\varphi \cos\varphi \sin\lambda, \quad (45)$$

$$u = -v_0 \sin\lambda \sin\varphi(4\cos^2\varphi - 1), \quad \text{and} \quad (46)$$

$$v = v_0 \sin^2\varphi \cos\lambda, \quad (47)$$

where $gh_0 = 5.768 \times 10^4$ m^2 s^{-1} and $v_0 = 20$ m s^{-1}.

In this test, a $32 \times 96 \times 2$ grid is employed. We have run with the time steps of 10 min (as the reference) and 30 min separately. The numerical results are plotted in Fig. 7 and Fig. 8, respectively. Both the results look very similar to McDonald and Bates's (1989) reference solution. When the time step is 30 min, the effective CFL number in terms of the gravity wave is about 1.6. It means that the present model is robust and works well even with a large time step for the fast waves. It should also be noted that since the quadrature for numerical flux is computed from the sample points along the trajectories, more sample points are needed to maintain high accuracy and stability when a larger CFL number is used. In practice, a CFL not much larger than unity is desirable.

e. Steady-state geostrophic flow

Similar to the test case 2 in Williamson et al. (1992), a steady geostrophic flow is specified with the initial velocity and height fields as

$$u = u_0(\cos\varphi \cos\alpha + \cos\lambda \sin\varphi \sin\alpha), \quad (48)$$

$$v = -u_0 \sin\lambda \sin\alpha \quad \text{and} \quad (49)$$

$$gh = gh_0 - \left(a\Omega u_0 + \frac{u_0^2}{2}\right)(-\cos\lambda \cos\varphi \sin\alpha + \sin\varphi \cos\alpha)^2, \quad (50)$$

where a is the Earth radius, $\Omega = 7.292 \times 10^{-5}$ s^{-1} is the rotation rate of Earth, $u_0 = 2\pi r_a/(12 \text{ days})$, and $gh_0 = 2.94 \times 10^4$ m^2 s^{-2}. The Coriolis parameter associated with this solution is $f = 2\Omega(-\cos\lambda \cos\varphi \sin\alpha + \sin\varphi \cos\alpha)$.

The 5-day integration results and the corresponding differences between the numerical solution and exact solution with $32 \times 96 \times 2$ cells are shown in Fig. 9 for different angles. The normalized error and convergence rate along different angles are shown in Tables 7–9. It is observed that more significant numerical errors are produced when the flow is in the zonal direction. This is due to the structure of the Yin–Yang boundary. A zonal flow passes through the longest boundary of the Yang grid, thus mostly affected by the numerical errors from the interpolation for communicating data across the Yin–Yang boundary. The numerical result after 5 days with the time step of 1200 s is also shown in Fig. 10 along the equatorial direction. In this case, our model still converges with an overall rate higher than second order when the refined grid is used. Considering the second-order central differencing used to discretize the Helmholtz equation, we may accept this as a reasonable result.

f. Zonal flow over an isolated mountain

This is case 5 suggested in the benchmark test set of Williamson et al. (1992). The initial velocity and height fields are the same as in the previous test with $u_0 = 20$ m s^{-1} and $h_0 = 5960$ m. The surface mountain height is given by

$$h = h_{s_0}(1 - r/R), \quad (51)$$

where $h_{s_0} = 2000$ m, $R = \pi/9$, and $r^2 = \min[R^2, (\lambda - \lambda_c)^2 + (\varphi - \varphi_c)^2]$. Here (λ_c, φ_c) is the center of the mountain located at $(3/2\pi, 1/6\pi)$ in this test.

With resolution of $80 \times 240 \times 2$ and time step of 200 s, our simulated results at day 5, 10, and 15 (shown in the left panels of Fig. 11) look quite similar to those from a spectral simulation of T213 (Jakob et al. 1993, p. 37). For comparison with spectral results, we repeat the simulation on the same resolution by using the Spectral-Transform Shallow-Water Model (STSWM) of Jakob et al. (1993, p. 37). The differences with the STSWM solution of height field on days 5, 10, and 15 are shown in the right panels of Fig. 11. As expected, the largest difference is found near the mountain. In fact, it is observed that spurious oscillations in the vicinity of the mountain at all resolutions are exhibited in the STSWM (Jakob et al. 1993, p. 37). In our model, however, the topographic source term is formulated in a well-balanced way with the gradient force term as discussed in Xing and Shu (2005). There is not noticeable spurious oscillations near the mountain in our results.

The relative variation in the total mass up to 15 days is plotted (see Fig. 13). We have a relative error in the total mass over the whole sphere with a magnitude of 10^{-4}%. Nevertheless, as mentioned earlier, with the mass exactly conserved on each individual component grid by CIP/MM FVM and the minimized overlapping zone where the numerical conservation is not rigorously guaranteed, the resulting numerical model has a conservativeness adequate for at least the medium-range weather prediction.

g. Rossby–Haurwitz wave

The zonally transported Rossby–Haurwitz wave, as the test 6 in Williamson et al. (1992), is widely used to

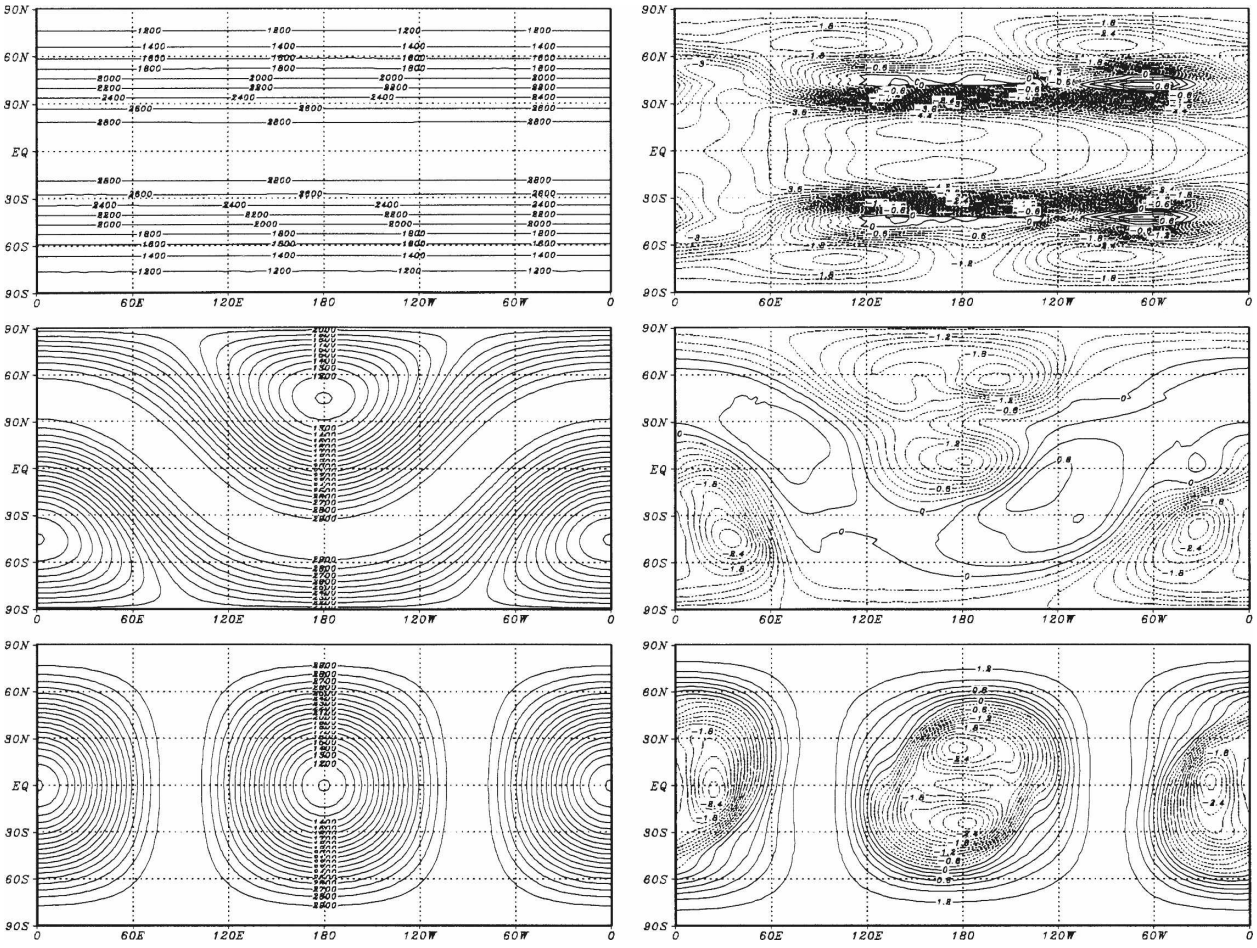

FIG. 9. Numerical solution for test case 2 in Williamson et al. (1992) after 5 days with (top left) $\alpha = 0$, (middle left) $\alpha = \pi/4$, and (bottom left) $\alpha = \pi/2$. (right) The corresponding differences between the numerical solution and exact solution. All contour intervals are of the difference of 0.2 m and the corresponding contours are (top right) from -4.6 to 0.8 m, (middle right) from -2.6 to 0.6 m, and (bottom right) from -2.6 to 1.2 m. Here $\Delta t = 600$ s and $c = 3.0 \times 10^6$ m^2 s^{-1} are used.

TABLE 7. Normalized errors and convergence rates of case 2 in Williamson et al. (1992) for $\alpha = 0.0$ and $c = 3.0 \times 10^6$.

Resolution	ℓ_1	ℓ_1 order	ℓ_2	ℓ_2 order	ℓ_∞	ℓ_∞ order
$16 \times 48 \times 2$	3.30×10^{-3}	—	4.44×10^{-3}	—	1.72×10^{-2}	—
$32 \times 96 \times 2$	6.67×10^{-4}	2.31	7.91×10^{-4}	2.49	2.81×10^{-3}	2.61
$64 \times 192 \times 2$	3.09×10^{-4}	1.11	3.41×10^{-4}	1.21	4.86×10^{-4}	2.53

TABLE 8. As in Table 7, but for $\alpha = \pi/4$.

Resolution	ℓ_1	ℓ_1 order	ℓ_2	ℓ_2 order	ℓ_∞	ℓ_∞ order
$16 \times 48 \times 2$	1.48×10^{-3}	—	1.69×10^{-3}	—	5.74×10^{-3}	—
$32 \times 96 \times 2$	3.27×10^{-4}	2.17	3.74×10^{-4}	2.18	7.49×10^{-4}	2.94
$64 \times 192 \times 2$	7.04×10^{-5}	2.21	8.24×10^{-5}	2.18	1.92×10^{-4}	1.96

TABLE 9. As in Table 7, but for $\alpha = \pi/2$

Resolution	ℓ_1	ℓ_1 order	ℓ_2	ℓ_2 order	ℓ_∞	ℓ_∞ order
$16 \times 48 \times 2$	1.79×10^{-3}	—	1.95×10^{-3}	—	2.80×10^{-3}	—
$32 \times 96 \times 2$	4.41×10^{-4}	2.02	4.84×10^{-4}	2.01	7.29×10^{-4}	1.94
$64 \times 192 \times 2$	9.52×10^{-5}	2.21	1.07×10^{-4}	2.18	1.87×10^{-4}	1.96

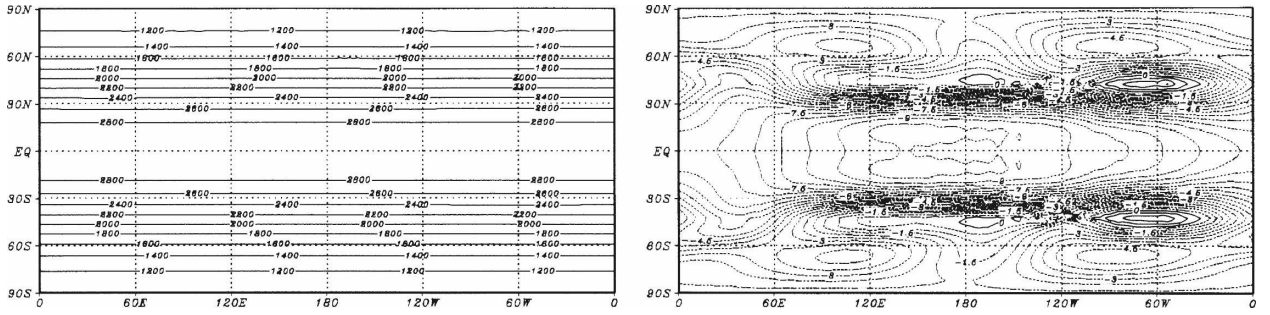

FIG. 10. As in Fig. 9, but with $\Delta t = 1200$ s, $\alpha = 0.0$, and $c = 3.0 \times 10^6$ m^2 s^{-1}.

validate the global models. The initial velocity component and height fields are given by

$$u = a\omega \cos\varphi + aK \cos^{R-1}\varphi(R \sin^2\varphi - \cos^2\varphi) \cos R\lambda, \tag{52}$$

$$v = -aKR \cos^{R-1}\varphi \sin\varphi \sin R\lambda, \quad \text{and} \tag{53}$$

$$gh = gh_0 + a^2A(\varphi) + a^2B(\varphi) \cos R\lambda + a^2C(\varphi) \cos 2R\lambda, \tag{54}$$

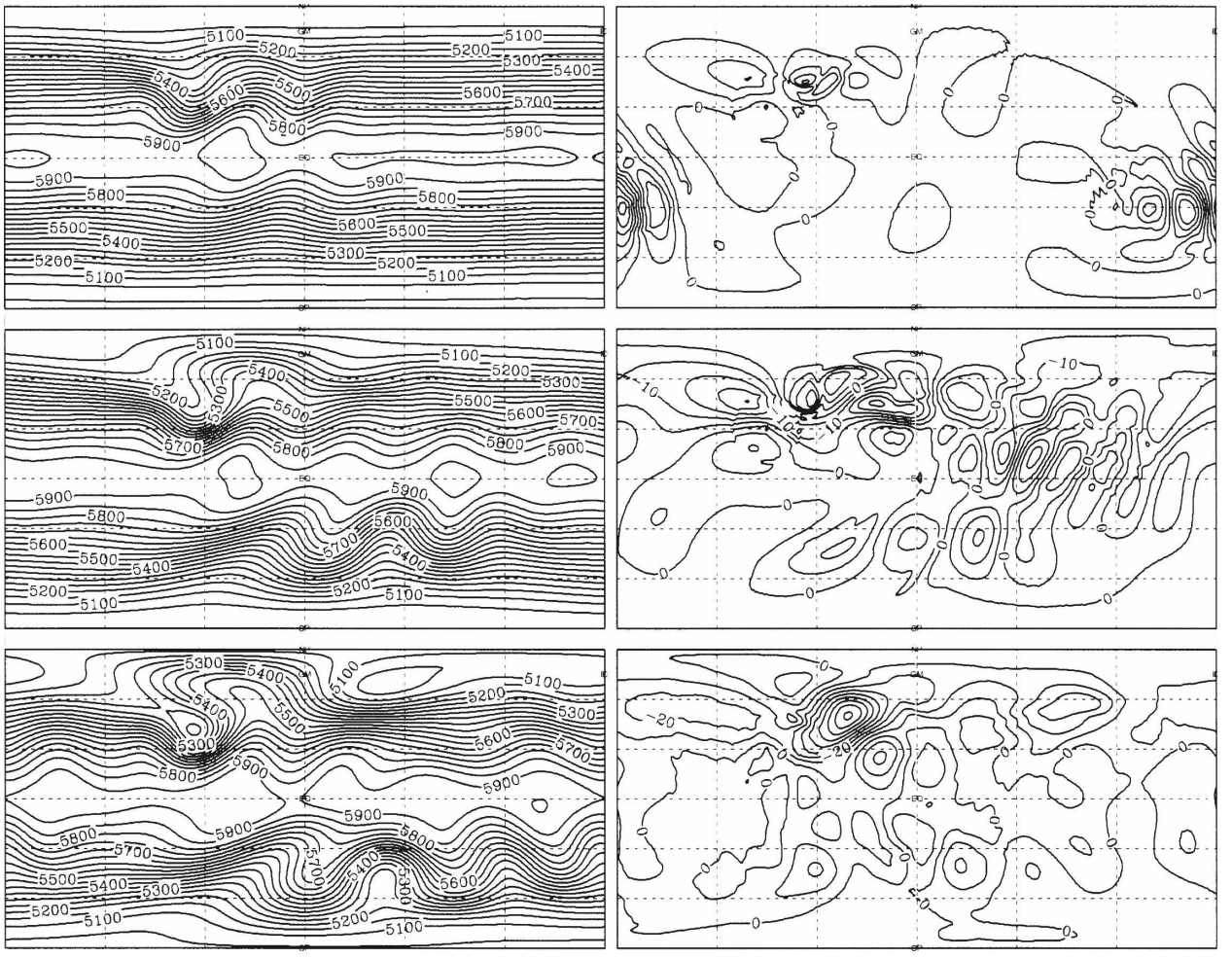

FIG. 11. Numerical solution for test case 5 in Williamson et al. (1992) at (top left) 5, (middle left) 10, and (bottom left) 15 days. (right) The corresponding differences with spectral solution on the same resolution. The contour interval of the difference of (top right) days 5 and (middle right) 10 is 5 m and that of (bottom right) day 15 is 10 m. Here $\Delta t = 200$ s, $\Delta\lambda = \Delta\varphi = 1.125°$, and $c = 6.8 \times 10^6$ m^2 s^{-1} are used.

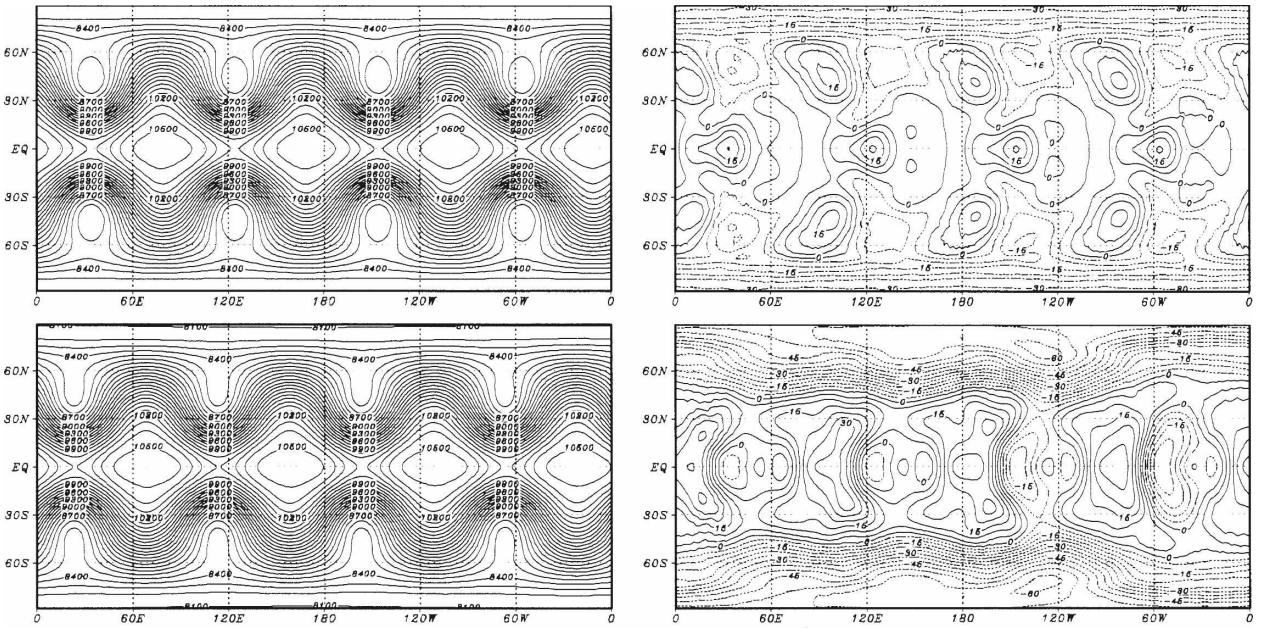

FIG. 12. Numerical solution for test case 6 in Williamson et al. (1992) at (top left) 7 and (bottom left) 14 days. (right) The corresponding differences with spectral solution on the same resolution. All contour intervals of difference are 5 m and the corresponding contours are (top right) from −30 to 20 m and (bottom right) from −60 to 30 m. We specified $\Delta t = 150$ s, $\Delta\lambda = \Delta\varphi = 1.875°$, and $c = 1.1 \times 10^7$ m^2 s^{-1} in the simulations.

where

$$A(\varphi) = \frac{\omega}{2}(2\Omega + \omega)\cos^2\varphi + \frac{1}{4}K^2\cos^{2R}\varphi[(R+1)\cos^2\varphi + (2R^2 - R - 2) - 2R^2\cos^{-2}\varphi],$$

$$B(\varphi) = \frac{2(\Omega + \omega)K}{(R+1)(R+2)}\cos^R\varphi[(R^2 + 2R + 2) - (R+1)^2\cos^2\varphi], \quad \text{and}$$

$$C(\varphi) = \frac{1}{4}K^2\cos^{2R}\varphi[(R+1)\cos^2\varphi - (R+2)].$$

We specify in this test $\omega = K = 7.848 \times 10^{-6}$ s^{-1}, $h_0 = 8 \times 10^3$ m, and $R = 4$.

In this test, we used a $48 \times 144 \times 2$ Yin–Yang grid that has a spatial resolution equivalent to T63 ($1.875° \times 1.875°$). The numerical results of the height field at 7 and 14 days are plotted in the left panel of Fig. 12. It is observed that the structure of a four-wave chain propagates zonally. Carefully examining the fine structures of the numerical solution, we find that our numerical output looks quite close to that of Jakob et al. (1993, p. 37) with a high resolution (T213). To compare the results with spectral solution, we repeated the simulation by the STSWM of Jakob et al. (1993, p. 37) with a T63 resolution. The differences between the two models are shown in the right panels of Fig. 12.

We plot the time evolution of the total mass in Fig. 13. Although the numerical conservation is currently not guaranteed in the Yin–Yang grid, the total mass variation up to 14 days in this case is negligibly small.

h. A more realistic case with the analyzed 500-mb height and wind field initial conditions

The last numerical test is a more realistic numerical experiment suggested as case 7 in Williamson et al. (1992). The initial conditions of height and wind are from the analysis of the 500-mb pressure surface at 0000 UTC 21 December 1978. We have computed these with both the CIP/MM FVM and the STSWM of Jakob et al. (1993, p. 37).

Figure 14 displays the height field from CIP/MM FVM after 5 days on a North Pole stereographic projection (left panel) with the resolution of T42 and time step 600s. The basic pattern is quite close to the spectral solution of STSWM (Jakob et al. 1993, p. 37) with the same resolution. The difference with the spectral solution of STSWM is shown in the right panel of Fig. 14. The simulation results of the South Pole are also presented in the Fig. 15. Again, the numerical results of CIP/MM FVM are in good agreement with the STSWM (Jakob et al. 1993, p. 37).

In this section, we have extensively conducted numerical benchmark tests to validate the present model. Shown above, the numerical results reveal that the model is computationally stable and robust, and exhib-

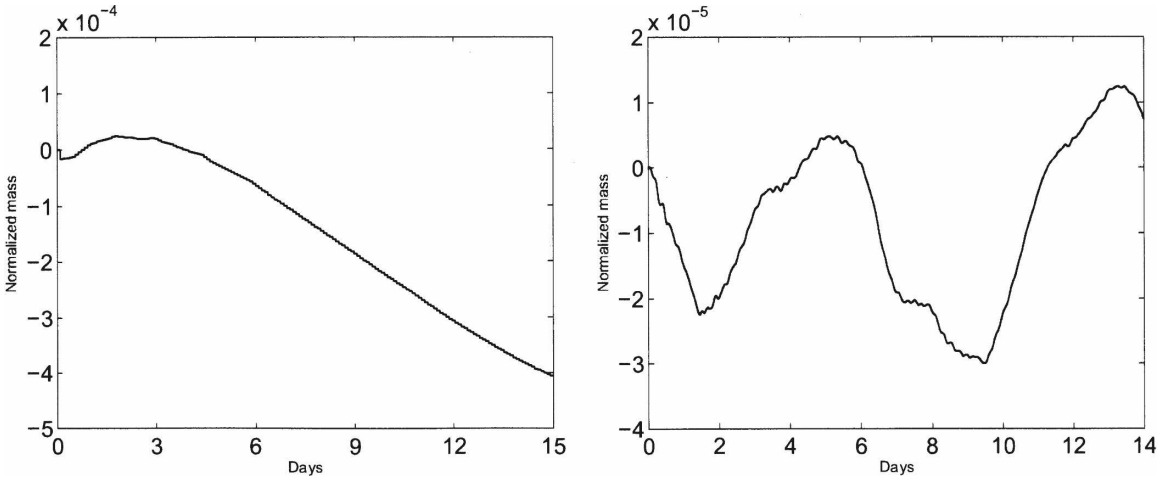

FIG. 13. The time evolution of the total mass in (left) case 5 and (right) case 6.

its competitive accuracy relative to other existing ones. We have never observed any computational mode from the numerical results in either the idealized or the realistic case, even when multimoments are involved in the numerical procedure.

7. Conclusions

We have developed a finite-volume model for shallow-water equations on the Yin–Yang spherical grid to get rid of the polar singularity and to explore the uniformity in grid spacing. A multimoment spatial discretization is used to get high-order interpolation reconstruction with compact grid stencil, hence, to minimize the overlapping region where the numerical conservativeness is not guaranteed. The PV moments are updated by a semi-implicit semi-Lagrangian approach to maintain the computational efficiency, whereas the VIA moments are computed through a flux-based finite-volume formulation to get the exact numerical conservation on each individual grid component. Even though we have only tried the semi-implicit semi-Lagrangian method of McDonald and Bates (1989) in the present paper, the concept of including an extra moment (i.e., the volume integrated value) to enforce the numerical conservativeness should be able to be applied to other semi-implicit semi-Lagrangian formu-

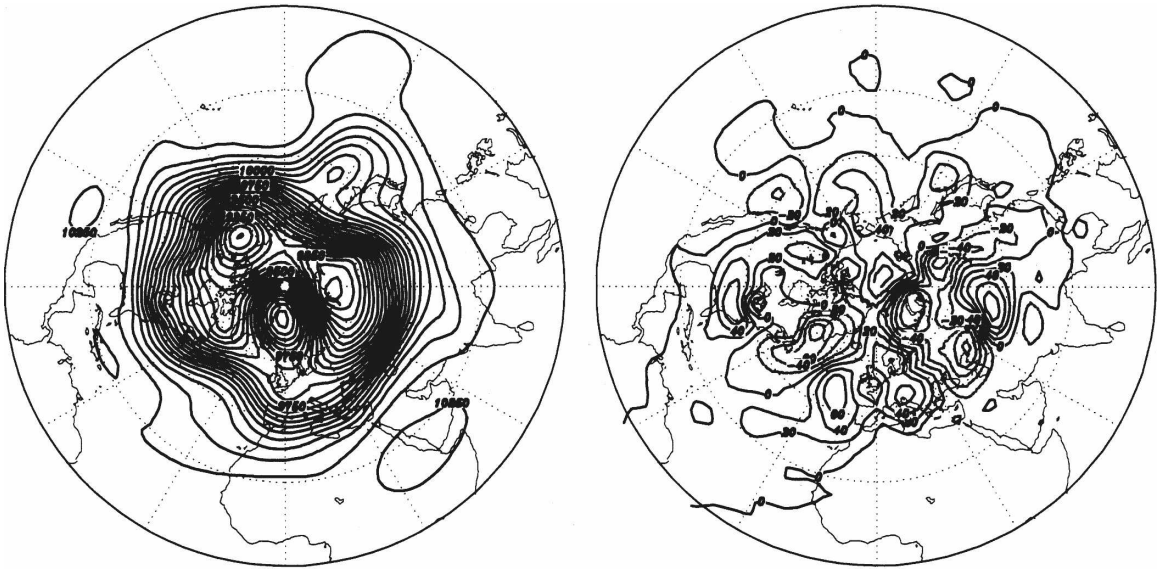

FIG. 14. (left) Height field for day 5 of the 21 Dec 1978 case on the North Pole stereographic projection. The contour interval is 50 m. (right) The difference with a spectral solution on the same resolution. The contour is from −100 to 80 m by 20 m. We specified $\Delta t = 600$ s, $\Delta\lambda = \Delta\varphi = 2.8125°$, and $c = 8.5 \times 10^6$ m^2 s^{-1} in this case.

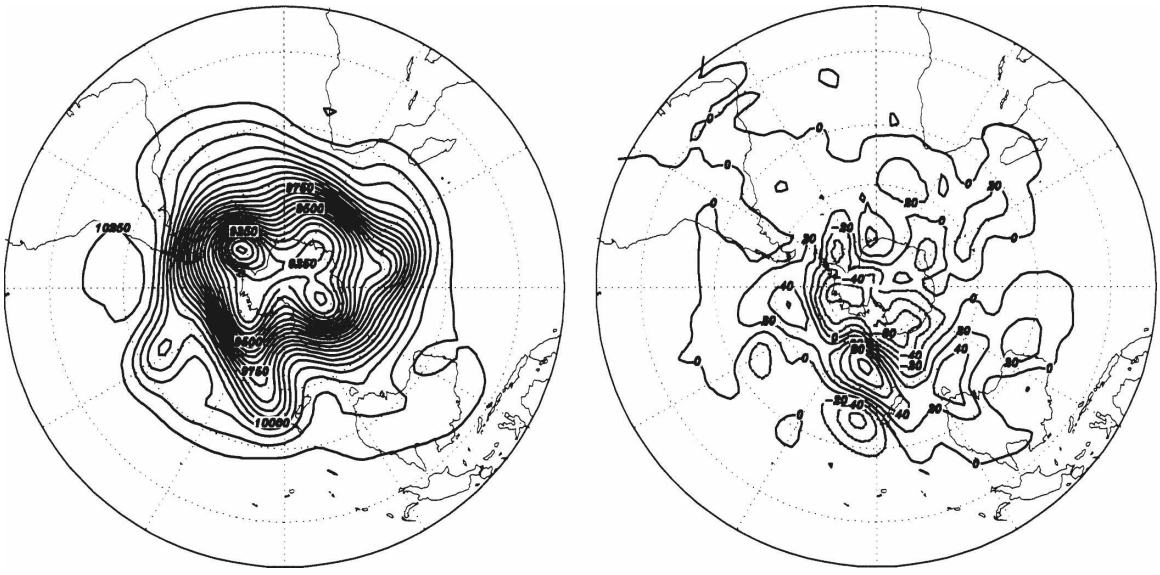

FIG. 15. As in Fig. 14, but over the South Pole. (right) The contour is from −60 to 100 m by 20 m.

lations that usually do not possess numerical conservativeness.

The numerical tests show that the present model has competitive numerical accuracy and computational efficiency even in the presence of fast wave. The conservation in total mass is adequate for at least the medium-range weather predictions or short-range climate simulations.

The numerical techniques presented in this paper constitute a promising and practical numerical framework to develop atmospheric and oceanic GCMs in spherical geometry.

Acknowledgments. The authors gratefully acknowledge the anonymous reviewers for their constructive comments on the manuscript, particularly for the careful examination on the dispersion relation of the M grid in Xiao et al. (2006b).

APPENDIX

Determination of the Coefficient in Multimoment Spatial Reconstruction

Shown in Fig. 2, we define two kinds of moments, that is the volume-integrated average and the point value, respectively, for the field variable $\Phi(\xi, \eta)$. Based on one VIA and eight PVs, we build a 2D quadratic polynomial for interpolation construction $F_{i,j}(\xi, \eta)$ [given by Eq. (13)] over the single cell Ω_{ij}.

From the constraint conditions

$$F_{i,j}(\xi_{i-1/2}, \eta_{j-1/2}) = \overline{{}^{P}\Phi}_{i-1/2,j-1/2}, \tag{A1}$$

$$F_{i,j}(\xi_{i}, \eta_{j-1/2}) = \overline{{}^{P}\Phi}_{i,j-1/2}, \tag{A2}$$

$$F_{i,j}(\xi_{i+1/2}, \eta_{j-1/2}) = \overline{{}^{P}\Phi}_{i+1/2,j-1/2}, \tag{A3}$$

$$F_{i,j}(\xi_{i-1/2}, \eta_{j}) = \overline{{}^{P}\Phi}_{i-1/2,j}, \tag{A4}$$

$$F_{i,j}(\xi_{i+1/2}, \eta_{j}) = \overline{{}^{P}\Phi}_{i+1/2,j}, \tag{A5}$$

$$F_{i,j}(\xi_{i-1/2}, \eta_{j+1/2}) = \overline{{}^{P}\Phi}_{i-1/2,j+1/2}, \tag{A6}$$

$$F_{i,j}(\xi_{i}, \eta_{j+1/2}) = \overline{{}^{P}\Phi}_{i,j+1/2}, \tag{A7}$$

$$F_{i,j}(\xi_{i+1/2}, \eta_{j+1/2}) = \overline{{}^{P}\Phi}_{i+1/2,j+1/2}, \quad \text{and} \tag{A8}$$

$$\frac{1}{\Delta\xi_i \Delta\eta_j} \int_{\xi_{i-1/2}}^{\xi_{i+1/2}} \int_{\eta_{j-1/2}}^{\eta_{j+1/2}} F_{i,j}(\xi,\eta)\, d\xi\, d\eta = \overline{{}^{V}\Phi}_{i,j}, \tag{A9}$$

the interpolation function in Eq. (13) can be uniquely determined, and the coefficients are

$$C_{00} = \overline{{}^{P}\Phi}_{i-1/2,j-1/2}, \tag{A10}$$

$$C_{10} = (4\overline{{}^{P}\Phi}_{i,j-1/2} - 3C_{00} - \overline{{}^{P}\Phi}_{i+1/2,j-1/2})/\Delta\xi_i, \tag{A11}$$

$$C_{20} = (2C_{00} + 2\overline{{}^{P}\Phi}_{i+1/2,j-1/2} - 4\overline{{}^{P}\Phi}_{i,j-1/2})/(\Delta\xi_i)^2, \tag{A12}$$

$$C_{01} = (4\overline{{}^{P}\Phi}_{i-1/2,j} - 3C_{00} - \overline{{}^{P}\Phi}_{i-1/2,j+1/2})/\Delta\eta_j, \tag{A13}$$

$$C_{02} = (2C_{00} + 2\overline{{}^{P}\Phi}_{i-1/2,j+1/2} - 4\overline{{}^{P}\Phi}_{i-1/2,j})/(\Delta\eta_j)^2, \tag{A14}$$

$$C_{11} = 2(4\overline{{}^{P}\Phi}_{i-1/2,j-1/2} + \overline{{}^{P}\Phi}_{i+1/2,j-1/2} + 18\overline{{}^{V}\Phi}_{i,j} - 8\overline{{}^{P}\Phi}_{i-1/2,j} + \overline{{}^{P}\Phi}_{i-1/2,j+1/2} - 8\overline{{}^{P}\Phi}_{i,j-1/2} - 4\overline{{}^{P}\Phi}_{i,j+1/2} - 4\overline{{}^{P}\Phi}_{i+1/2,j})/(\Delta\xi_i\Delta\eta_j), \tag{A15}$$

$$C_{12} = -(5\overline{{}^{P}\Phi}_{i-1/2,j-1/2} + \overline{{}^{P}\Phi}_{i+1/2,j-1/2} + 36\overline{{}^{V}\Phi}_{i,j} - 16\overline{{}^{P}\Phi}_{i-1/2,j} + 5\overline{{}^{P}\Phi}_{i-1/2,j+1/2} - 12\overline{{}^{P}\Phi}_{i,j-1/2} - 12\overline{{}^{P}\Phi}_{i,j+1/2} + \overline{{}^{P}\Phi}_{i+1/2,j+1/2} - 8\overline{{}^{P}\Phi}_{i+1/2,j})/[\Delta\xi_i(\Delta\eta_j)^2], \tag{A16}$$

$$C_{21} = -(5\overline{{}^{P}\Phi}_{i-1/2,j-1/2} - 16\overline{{}^{P}\Phi}_{i,j-1/2} + 5\overline{{}^{P}\Phi}_{i+1/2,j-1/2} - 12\overline{{}^{P}\Phi}_{i-1/2,j} + 36\overline{{}^{V}\Phi}_{i,j} - 12\overline{{}^{P}\Phi}_{i+1/2,j} + \overline{{}^{P}\Phi}_{i-1/2,j+1/2} - 8\overline{{}^{P}\Phi}_{i,j+1/2} + \overline{{}^{P}\Phi}_{i+1/2,j+1/2})/[(\Delta\xi_i)^2\Delta\eta_j], \quad \text{and} \tag{A17}$$

$$C_{22} = 3(\overline{{}^{P}\Phi}_{i+1/2,j-1/2} + 12\overline{{}^{V}\Phi}_{i,j} - 4\overline{{}^{P}\Phi}_{i-1/2,j} + \overline{{}^{P}\Phi}_{i-1/2,j+1/2} - 4\overline{{}^{P}\Phi}_{i,j-1/2} - 4\overline{{}^{P}\Phi}_{i,j+1/2} + \overline{{}^{P}\Phi}_{i-1/2,j-1/2} + \overline{{}^{P}\Phi}_{i+1/2,j+1/2} - 4\overline{{}^{P}\Phi}_{i+1/2,j})/(\Delta\xi_i\Delta\eta_j)^2. \tag{A18}$$

REFERENCES

Giraldo, F. X., and T. E. Rosmond, 2004: A scalable spectral element Eulerian atmospheric model (SEE-AM) for NWP: Dynamical core test. *Mon. Wea. Rev.,* **132,** 133–153.

Heikes, R. H., and D. A. Randall, 1995: Numerical integration of the shallow-water equations on a twisted icosahedral grid. Part I: Basic design and results of tests. *Mon. Wea. Rev.,* **123,** 1862–1880.

Ii, S., and F. Xiao, 2007: CIP/multi-moment finite volume method for Euler equations: A semi-Lagrangian characteristic formulation. *J. Comput. Phys.,* **222,** 849–871.

Jakob, R., J. J. Hack, and D. L. Williamson, 1993: Solutions to the shallow water test set using the spectral transform method. NCAR Tech. Note NCAR/TN-388+STR, National Center for Atmospheric Research, Boulder, CO, 82 pp.

Kageyama, A., and T. Sato, 2004: The "Yin-Yang grid": An overset grid in spherical geometry. *Geochem. Geophys. Geosyst.,* **5,** Q09005, doi:10.1029/2004GC000734.

Lauritzen, P. H., E. Kaas, and B. Machenhauer, 2006: A mass-conservative semi-implicit semi-Lagrangian limited area shallow water model on the sphere. *Mon. Wea. Rev.,* **134,** 1205–1221.

Li, X., D. Chen, X. Peng, F. Xiao, and X. Chen, 2006: Implementation of the semi-Lagrangian advection scheme on a quasi-Uniform overset Grid on a sphere. *Adv. Atmos. Sci.,* **23,** 792–801.

Lin, S.-J., and R. B. Rood, 1996: Multidimensional flux-form semi-Lagrangian transport schemes. *Mon. Wea. Rev.,* **124,** 2046–2070.

Majewski, D., and Coauthors, 2002: The operational global icosahedral–hexagonal gridpoint model GME: Description and high-resolution tests. *Mon. Wea. Rev.,* **130,** 319–338.

McDonald, A., and J. R. Bates, 1987: Improving the estimate of the departure point position in a two-time-level semi-Lagrangian and semi-implicit model. *Mon. Wea. Rev.,* **115,** 737–739.

——, and ——, 1989: A Semi-Lagrangian integration of a gridpoint shallow water model on the sphere. *Mon. Wea. Rev.,* **117,** 130–137.

McGregor, J. K., 1997: Semi-Lagrangian advection on a cubic gnomonic projection of the sphere. *Numerical Methods in Atmospheric and Oceanic Modelling: The André J. Robert Memorial Volume,* R. L. Charles, A. Lin, and H. Ritchie, Eds., CMOS/NRC Research Press, 153–169.

Nair, R. D., and B. Machenhauer, 2002: The mass conservative cell-integrated semi-Lagrangian advection scheme on the sphere. *Mon. Wea. Rev.,* **130,** 649–667.

——, J. Côté, and A. Staniforth, 1999: Cascade interpolation for semi-Lagrangian advection over the sphere. *Quart. J. Roy. Meteor. Soc.,* **125,** 1445–1468.

——, S. J. Thomas, and R. D. Loft, 2005a: A discontinuous Galerkin global shallow water model. *Mon. Wea. Rev.,* **133,** 876–888.

——, ——, and ——, 2005b: A discontinuous Galerkin transport scheme on the cubed sphere. *Mon. Wea. Rev.,* **133,** 814–828.

Peng, X., F. Xiao, and K. Takahashi, 2006: Conservative constraint for a quasi-uniform overset grid on sphere. *Quart. J. Roy. Meteor. Soc.,* **132,** 979–996.

Press, W. H., B. P. Flannery, S. A. Teukolsky, and W. T. Vetterling, 1992: Successive Over-relaxation (SOR). *Numerical Recipes in FORTRAN: The Art of Scientific Computing,* 2nd ed. Cambridge University Press, 866–869.

Qaddouri, A., L. Laayouni, S. Loisel, J. Côté, and M. Gander, 2007: Optimized Schwarz methods with an overset grid for the shallow-water equations: Preliminary results. *Appl. Numer. Math.,* **58,** 459–471, doi:10.1016/j.apnum.2007.01.015.

Rančić, M., J. Purser, and F. Mesinger, 1996: A global shallow-water model using an expanded spherical cube: Gnomonic versus conformal coordinates. *Quart. J. Roy. Meteor. Soc.,* **122,** 959–982.

Rasch, P. R., 1994: Conservative shape-preserving two-dimensional transport on a spherical reduced grid. *Mon. Wea. Rev.,* **122,** 1337–1350.

Ritchie, H., 1985: Application of a semi-Lagrangian integration scheme to the moisture equation in a regional forecast model. *Mon. Wea. Rev.,* **113,** 424–435.

Robert, A., 1981: A stable numerical integration scheme for the primitive meteorological equation. *Atmos.–Ocean,* **19,** 35–46.

——, 1982: Semi-Lagrangian and semi-implicit numerical integration scheme for the primitive meteorological equation. *J. Meteor. Soc. Japan,* **60,** 319–324.

Ronchi, C., R. Iacono, and P. S. Paolucci, 1996: The "cubed sphere": A new method for the solution of partial differential equations in spherical geometry. *J. Comput. Phys.,* **124,** 93–114.

Rossmanith, J. A., 2006: A wave propagation method for hyperbolic systems on the sphere. *J. Comput. Phys.,* **213,** 629–658.

——, A. Derek, S. Bale, and R. J. Leveque, 2004: A wave propagation algorithm for hyperbolic systems on curved manifolds. *J. Comput. Phys.,* **199,** 631–662.

Sadourny, R., 1972: Conservative finite-difference approximations of the primitive equations on quasi-uniform spherical grids. *Mon. Wea. Rev.,* **100,** 136–144.

Staniforth, A., and J. Côté, 1991: Semi-Lagrangian integration schemes for atmospheric models—A review. *Mon. Wea. Rev.,* **119,** 2206–2223.

Stuhne, G. R., and W. R. Peltier, 1999: New icosahedral grid-point discretizations of the shallow water equations on the sphere. *J. Comput. Phys.,* **148,** 23–58.

Thomas, S. J., and R. D. Loft, 2002: Semi-implicit spectral element model. *J. Sci. Comput.,* **17,** 339–350.

Tomita, H., M. Tsugawa, M. Satoh, and K. Goto, 2001: Shallow water model on a modified icosahedral geodesic grid by using spring dynamics. *J. Comput. Phys.,* **174,** 579–613.

Wesseling, P., 1991: *An Introduction to Multigrid Methods.* John Wiley & Sons, 283 pp.

Wiin-Nielsen, A., 1959: On the application of trajectory methods in numerical forecasting. *Tellus,* **11,** 180–196.

Williamson, D. L., J. B. Drake, J. J. Hack, R. Jackob, and P. N. Swarztrauber, 1992: A standard test for numerical approximations to the shallow water equations in spherical geometry. *J. Comput. Phys.,* **102,** 211–224.

Xiao, F., 2004: Unified formulation for compressible and incompressible flows by using multi-integrated moments. I: One-dimensional inviscid compressible flow. *J. Comput. Phys.,* **195,** 629–654.

——, and T. Yabe, 2001: Completely conservative and oscillationless semi-Lagrangian schemes for advection transportation. *J. Comput. Phys.,* **170,** 498–522.

——, R. Akoh, and S. Ii, 2006a: Unified formulation for compressible and incompressible flows by using multi integrated moments. II: Multi-dimensional version for compressible and incompressible flows. *J. Comput. Phys.,* **213,** 31–56.

——, X. Peng, and X. Shen, 2006b: A finite volume grid using multi-moments for geostrophic adjustment. *Mon. Wea. Rev.,* **134,** 2515–2526.

Xing, Y., and C. W. Shu, 2005: High order finite difference WENO schemes with the exact conservation property for the shallow water equations. *J. Comput. Phys.,* **208,** 206–227.

Yabe, T., R. Tanaka, T. Nakamura, and F. Xiao, 2001: Exactly conservative semi-Lagrangian scheme (CIP-CSL) in one dimension. *Mon. Wea. Rev.,* **129,** 332–344.

Zerroukat, M., N. Wood, and A. Staniforth, 2004: SLICE-S: A semi-Lagrangian inherently conserving and efficient scheme for transport problems on the sphere. *Quart. J. Roy. Meteor. Soc.,* **130,** 2649–2664.